5

IMAGING RADAR POLARIMETRY

J. J. van Zyl and H. A. Zebker

The basic theory and the implementation of imaging radar polarimetry for the study of natural surfaces have been the subject of great interest in the recent past [Evans et al., 1986; Boerner et al., 1987; Borgeaud et al., 1987; Ulaby et al., 1987; van Zyl et al., 1987; Zebker et al., 1987, Evans et al., 1988; Swartz et al., 1988; Yueh et al., 1988; Agrawal and Boerner, 1989; Durden et al., 1989; Lim et al., 1989; van Zyl, 1989]. In this paper, we review the state of the art in imaging radar polarimetry, examine current developments in sensor technology and implementation for recording polarimetric measurements, and de-

scribe techniques and areas of application for the new remote sensing data.

Conventional imaging radars operate with a single, fixed-polarization antenna for both transmission and reception of radio frequency signals. In this way a single scattering coefficient is measured, for a specific transmit and receive polarization combination, for many thousands of points in a scene. A result of this implementation is that the scattered wave, a vector quantity, is measured as a scalar quantity, and any additional information about the surface contained in the polarization properties of the reflected signals is lost. To ensure that all the information in the scattered wave is retained, the polarization of the scattered wave must be measured through a vector measurement process. A device which measures the polarization properties of radiation is called a polarimeter, hence an imaging radar which permits measurement of the full polarization signature of every resolution element in an image is properly called an imaging radar polarimeter.

Recent developments in technology, most notably the availability of digital data recording and general purpose computers for data reduction, permit the implementation of full imaging radar polarimeters that measure the complete scattering matrix of an object (for a more complete description of the scattering matrix, see, for example, Born and Wolf [1980], van de Hulst [1981], or Jackson [1976]). Polarimetry, for the purposes of this paper, refers to instrumental techniques for the determination of the complex backscatter coefficients of radar echoes for any and all transmit and receive polarizations. It is thus an extension of scatterometry, in which the received power of an echo is typically recorded for one or more fixed polarization states and a single, or two orthogonal, transmit states. High-resolution, or imaging, polarimetry permits measurements of the amplitude and relative phase of all polarizations for transmit and receive. We have previously described one implementation of a polarimeter [Zebker et al., 1987], and additional airborne instruments are currently under development by NASA, the Canadian Centre for Remote Sensing, and the Environmental Research Institute of Michigan. These instruments are described in the appropriate section below. In addition, NASA is in the process of developing spaceborne polarimetric radar systems. The Shuttle Imaging Radar C (SIR-C) instrument represents the first application of this technology to a spaceborne sensor.

The theoretical basis for multipolarized radars was developed in

the 1950's by several groups, in particular Sinclair [1950], Rumsey, Deschamp, Kales and Bohnert (a series of papers in 1951), and the work of Kennaugh (thesis and several reports of the Ohio State Antenna Lab, from 1949 to 1954). This was followed by advances in instrumentation and by a series of experimental measurements for a variety of targets (for example, Copeland [1960], Long [1965], Hunter and Senior [1966], or Long and Zehner [1970]). Application to geological problems probably began with Hagfors' [1967] lunar studies; this work is notable also for the implementation of the ability to select arbitrary polarization states for the instrument. The theoretical approach to target description was continued by Huynen [1965, 1970, 1975, 1978] who addressed the problem of optimal polarization in a rigorous manner. Recently, the inverse scattering problem has been defined and investigated in some detail by Boerner [1981], Boerner et al. [1981], and Foo et al. [1984]; these and other results are summarized in a book edited by Boerner et al. [1985]. A general review of polarimetric radar technology prior to the advent of imaging radar polarimetry can be found in Giuli [1986].

5.1 Fundamental Theory of Radar Polarimetry

The basic datum measured by a polarimeter is a complex (amplitude and phase) scattering matrix for each very small resolution element of the radar. For reasons of data handling efficiency, several individual measurements are usually combined to form the Stokes matrix [van Zyl, 1985; van Zyl et al., 1987] or the covariance matrix (for example, Kong et al., [1987]) corresponding to that group of pixels. In this section we define our coordinate system and the scattering, Stokes, and covariance matrices. We then present the concept of polarization synthesis, which is a technique that allows implementation of imaging polarimeters. Finally, we introduce the polarization signature, a convenient graphical representation of the polarimetric behavior of an object. We shall first introduce these concepts for the general bistatic case and then discuss the important special case of backscatter.

a. Coordinate System

We express the transverse components of the electric field of a scattered wave according to the coordinate systems shown in Fig. 5.1. First, a global Cartesian coordinate system with basis vectors $\hat{\mathbf{x}}$, $\hat{\mathbf{y}}$

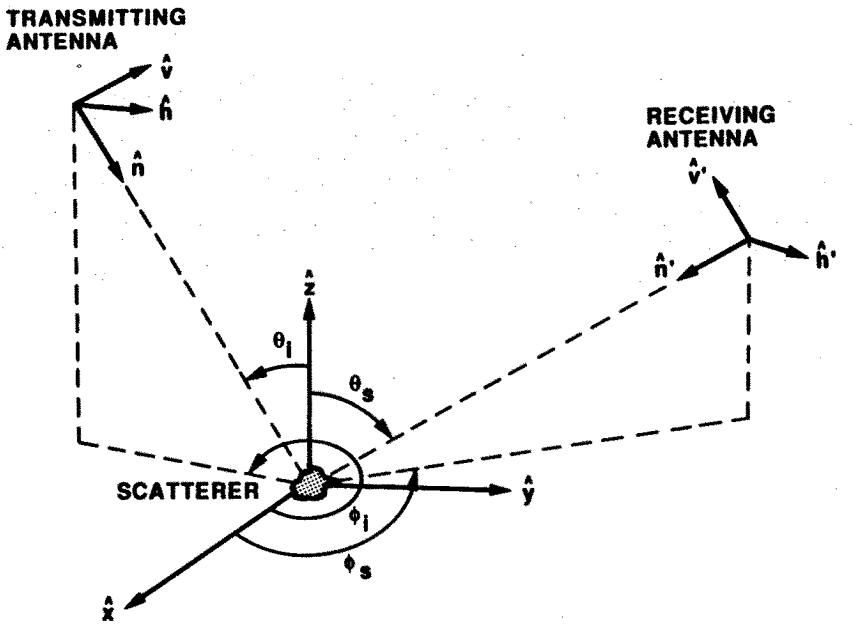

Figure 5.1 Scattering Geometry and Local Coordinate Systems.

and $\hat{\mathbf{z}}$ is set up with its origin within the scatterer. The transverse components of the electric field of the wave illuminating the scatterer are expressed in terms of a local Cartesian coordinate system $(\hat{\mathbf{h}}, \hat{\mathbf{v}}, \hat{\mathbf{n}})$ with its origin at the transmitting antenna. The basis vectors of this local coordinate system can be written in terms of the basis vectors of the global coordinate system as follows:

$$\hat{\mathbf{h}} = \sin(\phi_i)\hat{\mathbf{x}} - \cos(\phi_i)\hat{\mathbf{y}} \tag{1a}$$

$$\hat{\mathbf{v}} = -\cos(\phi_i)\cos(\theta_i)\hat{\mathbf{x}} - \sin(\phi_i)\cos(\theta_i)\hat{\mathbf{y}} + \sin(\theta_i)\hat{\mathbf{z}} \tag{1b}$$

$$\hat{\mathbf{n}} = -\cos(\phi_i)\sin(\theta_i)\hat{\mathbf{x}} - \sin(\phi_i)\sin(\theta_i)\hat{\mathbf{y}} - \cos(\theta_i)\hat{\mathbf{z}} \tag{1c}$$

The transverse components of the electric field of the scattered wave are expressed in terms of a second local coordinate system $(\hat{\mathbf{h}}', \hat{\mathbf{v}}', \hat{\mathbf{n}}')$ with its origin at the receiving antenna. To write the basis vectors of the primed coordinate system in terms of the basis vectors of the global coordinate system, one simply replaces the subscript i by a subscript s in (1). Note that this choice of coordinate systems ensures that the primed and unprimed coordinate systems coincide

when the receiving and transmitting antennas are located at the same point, i.e., in the backscatter case. We note that another common basis set is that consisting of right-and left-hand circular polarizations, and all of the analyses we present could be implemented using this, or any other, basis. We will use the linear basis here.

Using the coordinate systems described above, it is possible to write the transverse components of the electric field of the scattered wave in terms of the transverse components of the electric field of the illuminating wave using a complex 2 × 2 *scattering matrix* [Sinclair, 1950; Kennaugh, 1951; van de Hulst, 1981]

$$\begin{pmatrix} E_{h'} \\ E_{v'} \end{pmatrix}^{sc} = \frac{e^{ikr}}{kr} \begin{pmatrix} S_{h'h} & S_{h'v} \\ S_{v'h} & S_{v'v} \end{pmatrix} \begin{pmatrix} E_h \\ E_v \end{pmatrix}^{ill} \tag{2}$$

where the superscript *ill* represents the illuminating wave and the superscript *sc* represents the scattered wave. Here, r is the distance between the scatterer and the receiving antenna and k is the wavenumber of the illuminating wave. Each element of the scattering matrix may be a function of frequency and of the scattering and illuminating angles.

b. Polarization Synthesis

Knowledge of the scattering matrix [S] permits calculation of the received power for any possible combination of transmit and receive antennas; this process is called polarization synthesis [van Zyl et al., 1987; Zebker et al., 1987]. This important technique is what gives polarimetry its great advantage over conventional fixed-polarization radars — more information may be inferred about the surface if the full polarimetric properties are known.

The procedure for calculating the radar backscatter coefficient for any synthesized antenna pair is as follows. The power P observed if we were to utilize antennas with electric field vectors $\mathbf{E}_t$ and $\mathbf{E}_r$ for transmit and receive, respectively, is found by evaluating the matrix equation [van Zyl, 1985; van Zyl et al., 1987]

$$P = K(\lambda, \theta, \phi)|\mathbf{E}_r \cdot [\mathbf{S}]\mathbf{E}_t|^2 \tag{3}$$

where

$$K(\lambda, \theta, \phi) = \frac{1}{2} \frac{\lambda^2}{4\pi} \sqrt{\frac{\epsilon_0}{\mu_0}} \frac{g(\theta, \phi)}{|\mathbf{E}_r|^2}$$

and $g(\theta, \phi)$ is the antenna gain function, $(\lambda^2/4\pi)g(\theta, \phi)$ is the effective area of the antenna and ϵ_0 and μ_0 are the permittivity and

permeability of free space respectively.

Equations (2) and (3) are the fundamental equations of radar polarimetry [Kostinski and Boerner, 1986]. An imaging polarimeter is usually implemented by configuring the hardware to measure the four scattering matrix elements directly for every resolution element in a scene. (For a detailed description of a typical implementation, see Zebker et al., [1987])

Polarization synthesis can also be expressed in terms of either the Stokes matrix [M] [van Zyl et al., 1987] or the covariance matrix [C] [Swartz et al., 1988]. Both of these representations consist of linear combinations of the cross-products of the four basic elements of the scattering matrix. The definitions of the Stokes matrix [M] in the linear basis is [van Zyl, 1985; van Zyl et al., 1987]

$$[\mathbf{M}] = [\tilde{\mathbf{Q}}]^{-1}\,[\mathbf{A}]\,[\mathbf{Q}]^{-1} \tag{4}$$

where

$$[\mathbf{A}] = \begin{pmatrix} S_{h'h}\cdot S^*_{h'h} & S_{h'v}\cdot S^*_{h'v} & S_{h'h}\cdot S^*_{h'v} & S_{h'v}\cdot S^*_{h'h} \\ S_{v'h}\cdot S^*_{v'h} & S_{v'v}\cdot S^*_{v'v} & S_{v'h}\cdot S^*_{v'v} & S_{v'v}\cdot S^*_{v'h} \\ S_{h'h}\cdot S^*_{v'h} & S_{h'v}\cdot S^*_{v'v} & S_{h'h}\cdot S^*_{v'v} & S_{h'v}\cdot S^*_{v'h} \\ S_{v'h}\cdot S^*_{h'h} & S_{v'v}\cdot S^*_{h'v} & S_{v'h}\cdot S^*_{h'v} & S_{v'v}\cdot S^*_{h'h} \end{pmatrix}$$

and

$$[\mathbf{Q}] = \begin{pmatrix} 1 & 1 & 0 & 0 \\ 1 & -1 & 0 & 0 \\ 0 & 0 & 1 & i \\ 0 & 0 & 1 & -i \end{pmatrix}$$

$[\tilde{\mathbf{Q}}]$ means the transpose of the matrix $[\mathbf{Q}]$ and the asterisk denotes complex conjugation. The definition of the covariance matrix [C] is

$$[\mathbf{C}] = \begin{pmatrix} S_{h'h}\cdot S^*_{h'h} & S_{h'h}\cdot S^*_{h'v} & S_{h'h}\cdot S^*_{v'h} & S_{h'h}\cdot S^*_{v'v} \\ S_{h'v}\cdot S^*_{h'h} & S_{h'v}\cdot S^*_{h'v} & S_{h'v}\cdot S^*_{v'h} & S_{h'v}\cdot S^*_{v'v} \\ S_{v'h}\cdot S^*_{h'h} & S_{v'h}\cdot S^*_{h'v} & S_{v'h}\cdot S^*_{v'h} & S_{v'h}\cdot S^*_{v'v} \\ S_{v'v}\cdot S^*_{h'h} & S_{v'v}\cdot S^*_{h'v} & S_{v'v}\cdot S^*_{v'h} & S_{v'v}\cdot S^*_{v'v} \end{pmatrix} \tag{5}$$

The polarization synthesis expressions for the Stokes matrix and the covariance matrix are:

$$P = K(\lambda,\theta,\phi)\,\mathbf{S}_r\cdot[\mathbf{M}]\mathbf{S}_t, \tag{6}$$

where $\mathbf{S}_r$ and $\mathbf{S}_t$ are the Stokes vectors describing the polarizations of the receiving and transmitting antennas, respectively, and

$$P = K(\lambda, \theta, \phi)\, \mathbf{W}^* \cdot [\mathbf{C}]\mathbf{W} \tag{7}$$

$\mathbf{W}$ is a 4-dimensional complex vector with elements related to the electric fields of the transmitting and receiving antennas as follows:

$$\mathbf{W} = \begin{pmatrix} E_{hr}E_{ht} \\ E_{hr}E_{vt} \\ E_{vr}E_{ht} \\ E_{vr}E_{vt} \end{pmatrix}$$

For imaging radars, the individual power measurements for each radar resolution element are related only statistically, therefore, in a typical radar system several power measurements are added to reduce statistical variation at the expense of loss of spatial resolution. The total power received from a set of N measurements, then, can be expressed [van Zyl et al., 1987]

$$P = \sum_{n=1}^{N} P^{(n)} \tag{8}$$

where $P^{(n)}$ is the power received from the n^{th} individual measurement. Thus, if the same antennas are used for each observation and the multiplicative factor K is assumed constant over the averaging interval,

$$P = K(\lambda, \theta, \phi)\, \mathbf{S}_r \cdot \left(\sum_{n=1}^{N} [\mathbf{M}^{(n)}] \right) \mathbf{S}_t \tag{9}$$

or

$$P = K(\lambda, \theta, \phi)\, \mathbf{W}^* \cdot \left(\sum_{n=1}^{N} [\mathbf{C}^{(n)}] \right) \mathbf{W} \tag{10}$$

where, $[\mathbf{M}^{(n)}]$ and $[\mathbf{C}^{(n)}]$ are the Stokes matrix and the covariance matrix of the n^{th} measurement, respectively. We note that in terms of the scattering matrix, (8) can be written as

$$P = K(\lambda, \theta, \phi) \sum_{n=1}^{N} |\mathbf{E}_r \cdot [\mathbf{S}^{(n)}]\mathbf{E}_t|^2 \tag{11}$$

Equations (9)–(11) show the advantage of using the Stokes matrix or covariance matrix representations for polarization synthesis in the case of imaging radar polarimeters. Although the same information would be conveyed using (9), (10) or (11), the Stokes and covariance matrices have the additional advantage that the collective properties of a group of resolution elements can be expressed using a single matrix rather than requiring the individual scattering matrices for each element. In addition, the three different approaches also require different amounts of computations to synthesize the polarization signature for a collection of N pixels. For example, for the monostatic case, it can be shown that the Stokes matrix approach requires $10N$ real number additions to calculate the composite Stokes matrix, followed by 10 real number multiplications to synthesize the received power from this composite area for an arbitrary polarization combination. The covariance matrix approach requires $12N$ real number additions ($6N$ complex additions) and 24 real multiplications (6 complex multiplications) for the same synthesis procedure, while the scattering matrix approach requires $16N$ real multiplications ($4N$ complex multiplications) followed by N real additions. For large values of N, the Stokes matrix method will therefore require significantly fewer computations than the scattering matrix and covariance matrix methods.

Currently, both the Stokes and the covariance matrices are in use. Each has certain computational advantages depending on the particular application of the polarimeter, but identical results may be achieved with either representation. Note that there are at least two definitions of the covariance matrix in present use; we have given the more common definition here. The other definition is one used by Huynen [1985] that is applied to target decomposition problems.

c. Monostatic Polarimeters

Currently all imaging radar polarimeters operate in the monostatic mode, i.e., the transmit and receive antennas are at the same location in space. (Note that this does not mean that the transmit and receive antennas necessarily have the same polarization.) In this case, reciprocity dictates that $S_{h'v} = S_{v'h}$, resulting in a symmetrical scattering matrix. It is easily seen from (3) that if [S] is symmetrical, [A], and hence the Stokes matrix [M] will be symmetrical. In this case it can be shown [van Zyl et al., 1987] that for distributed scatterers, there are up to 9 independent parameters in the Stokes matrix. In terms of

the scattering matrix elements, the monostatic Stokes matrix elements are:

$$M_{11} = \frac{1}{4}[S_{hh} \cdot S_{hh}^* + S_{vv} \cdot S_{vv}^* + 2S_{hv} \cdot S_{hv}^*] \tag{12a}$$

$$M_{12} = \frac{1}{4}[S_{hh} \cdot S_{hh}^* - S_{vv} \cdot S_{vv}^*] \tag{12b}$$

$$M_{13} = \frac{1}{2}\Re[S_{hh}^* \cdot S_{hv}] + \frac{1}{2}\Re[S_{hv}^* \cdot S_{vv}] \tag{12c}$$

$$M_{14} = \frac{1}{2}\Im[S_{hh}^* \cdot S_{hv}] + \frac{1}{2}\Im[S_{hv}^* \cdot S_{vv}] \tag{12d}$$

$$M_{22} = \frac{1}{4}[S_{hh} \cdot S_{hh}^* + S_{vv} \cdot S_{vv}^* - 2S_{hv} \cdot S_{hv}^*] \tag{12e}$$

$$M_{23} = \frac{1}{2}\Re[S_{hh}^* \cdot S_{hv}] - \frac{1}{2}\Re[S_{hv}^* \cdot S_{vv}] \tag{12f}$$

$$M_{24} = \frac{1}{2}\Im[S_{hh}^* \cdot S_{hv}] - \frac{1}{2}\Im[S_{hv}^* \cdot S_{vv}] \tag{12g}$$

$$M_{33} = \frac{1}{2}S_{hv} \cdot S_{hv}^* + \frac{1}{2}\Re[S_{hh}^* \cdot S_{vv}] \tag{12h}$$

$$M_{34} = \frac{1}{2}\Im[S_{hh}^* \cdot S_{vv}] \tag{12i}$$

$$M_{44} = \frac{1}{2}S_{hv} \cdot S_{hv}^* - \frac{1}{2}\Re[S_{hh}^* \cdot S_{vv}] \tag{12j}$$

where $\Re$ and $\Im$ represent the real and imaginary parts of the subsequent quantities, respectively. Three of the ten parameters listed above are related through [Huynen, 1970; van Zyl et al., 1987]

$$M_{11} = M_{22} + M_{33} + M_{44} \tag{13}$$

In the backscatter case, the covariance matrix can be reduced to a Hermetian 3×3 matrix [Swartz et al., 1989]

$$[\mathbf{C}] = \begin{pmatrix} S_{hh} \cdot S_{hh}^* & S_{hh} \cdot S_{hv}^* & S_{hh} \cdot S_{vv}^* \\ S_{hv} \cdot S_{hh}^* & S_{hv} \cdot S_{hv}^* & S_{hv} \cdot S_{vv}^* \\ S_{vv} \cdot S_{hh}^* & S_{vv} \cdot S_{hv}^* & S_{vv} \cdot S_{vv}^* \end{pmatrix} \tag{14a}$$

and $\mathbf{W}$ reduces to a 3-dimensional complex vector with elements related to the electric fields of the transmitting and receiving antennas as follows:

$$\mathbf{W} = \begin{pmatrix} E_{hr}E_{ht} \\ E_{hr}E_{vt} + E_{vr}E_{ht} \\ E_{vr}E_{vt} \end{pmatrix} \tag{14b}$$

The polarization synthesis equations for the monostatic case are the same as those for the bistatic case.

We note that for the rest of this chapter, it is implicitly assumed that all of the radar systems described are monostatic, and all data and techniques presented are implemented with monostatic systems.

d. Polarization Signatures

A particular graphical representation of the variation of received power as a function of polarization known as the polarization signature [van Zyl, 1985; van Zyl et al., 1987; Zebker et al., 1987; Agrawal and Boerner, 1989] is quite useful for describing polarization properties of areas. The signature consists of a plot of synthesized radar cross-section as a function of the ellipticity and orientation angles of the transmit antenna; the signatures shown here also use the same antenna for receive. We illustrate two theoretical signatures in Fig. 5.2. One signature was generated using a second order small perturbation model for scattering by a slightly rough surface, while the second represents the theoretical signature of a perfectly conducting dihedral corner reflector [van Zyl et al., 1987]. These signatures are shaped quite differently as different scattering mechanisms are responsible for the backscatter in each case – the slightly rough surface return is due mainly to Bragg scattering, while the return from the dihedral corner reflector suffered two reflections.

Note that the polarization signature of the rough surface scattering appears to sit on a "pedestal." As pointed out before [van Zyl et al., 1987], this means that there is some portion of the return which cannot be nulled out simply by changing the polarization of the transmitting and receiving antennas. In polarimetric observations, the presence of a pedestal in the signature means that the individual measured scattering, Stokes or covariance matrices used to calculate the signature were not all identical. The more different the individual matrices, the higher the resulting pedestal. In radar images, this variation of scattering properties results from various different effects which all can cause the measured scattering, and hence Stokes or covariance, matrices of adjacent resolution elements to be slightly different. The first obvious cause of such a variation is when adjacent pixels really contain different types of scatterers. Other causes include diffuse (i.e., multiple) scattering and the presence of noise.

The polarization signatures of many different scatterers are de-

scribed by van Zyl et al., [1987], Zebker et al., [1987] and by Agrawal and Boerner [1989]. We shall discuss several polarization signatures observed with an imaging polarimeter in more detail in a later section.

e. Implications for Polarimetric Modeling

The new capabilities to measure in detail the polarimetric properties of terrain has accelerated interest in modeling of polarimetric behavior based on knowledge of the surface. This modeling effort permits comparison of measured and predicted properties, thus providing the means to interpret remotely-sensed data in ways not possible before radar polarimetry.

Many of the newer modeling approaches require extension of previous models to include calculation of both the amplitude and phase of the various cross-products of the scattering matrix elements that make up the Stokes or covariance matrix elements rather than simply the power measured by various antenna combinations. For example, scattering from slightly rough surfaces has been previously calculated for the σ_{hh} case by Rice [1953], for the σ_{vv} case by Peake [1959], and for the σ_{hv} case by Valenzuela [1967], but no cross-terms such as $S_{hh}S_{vv}^*$ were typically calculated. To fully model polarimetric scattering all the cross-products of the scattering matrix elements, i.e., the full Stokes or covariance matrix must be calculated.

Recently, Rice's small perturbation model was extended to the full polarimetric case [van Zyl et al., 1987], retaining scattered fields up to second order. It was shown that this model successfully predicts observed polarization signatures for scattering by the ocean surface and, surprisingly, relatively smooth lava fields at L-band, including the "pedestal" observed in the measured signatures. The model predicts that the height of the observed pedestal increases as the surface roughness increases. Examples of observed and predicted polarization signatures, extracted from [van Zyl et al., 1987] are presented in Fig. 5.3.

Many different models predicting the radar backscatter from earth terrain have been proposed in the literature. Here, we do not intend to describe all of these in detail. Instead, we propose to give a general overview of the main areas of focus. The three main approaches are used to model the polarimetric scattering from different types of earth terrain. These are the radiative transfer method, the random medium model and the discrete scatterer approach. In all cases, the scattering

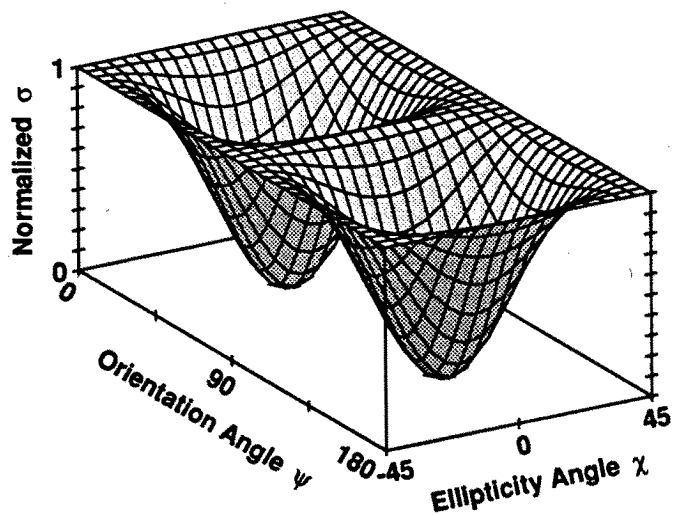

(a)

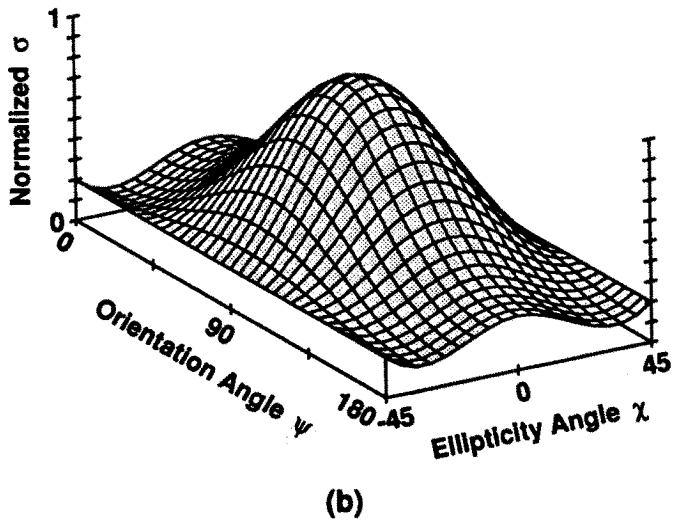

(b)

Figure 5.2 Co-polarized signature of a perfectly conducting dihedral corner reflector (a), and that of slightly rough surface scattering at an incidence angle of 50 degrees (b). The slightly rough surface is characterized by [van Zyl et al., 1987] $kh = .5$, r.m.s. slopes 30 degrees and dielectric constant 81.

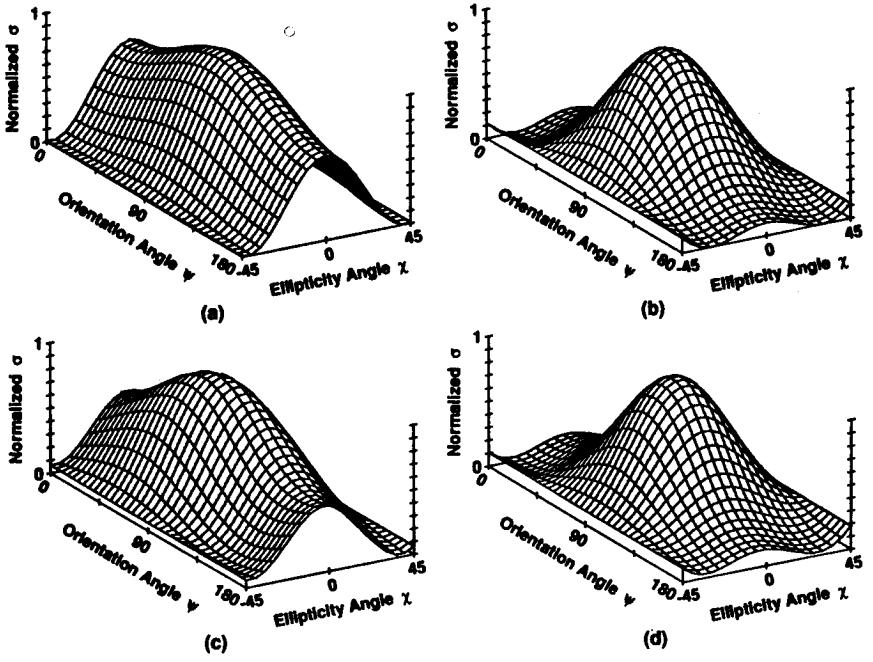

Figure 5.3 Theoretical co-polarized signatures for rough surface scattering at incidence angles of (a) 20 degrees and (b) 50 degrees. The surface is characterized by $kh = .1$, r.m.s. slopes 5 degrees and dielectric constant 81. Also shown are measured co-polarized signatures of the ocean at incidence angles of 20 degrees (c) and 50 degrees (d). (Extracted from van Zyl et al., [1987]).

medium is modeled as consisting of horizontal layers with different scattering properties. For example, forested areas are usually modeled using three layers, the top representing the branches and leaves or twigs, the middle representing the trunks and the bottom representing the ground surface.

The MIMICS model, derived at the University of Michigan [Ulaby et al., 1988], is an example of the application of radiative transfer methods to the modeling of radar backscatter from vegetated areas. This approach seems to yield good results, but the disadvantages include the many input parameters needed and especially the many computer operations needed per run.

In the random medium approach [Tsang et al., 1985], the medium is considered to be continuous and layered, with a randomly fluctuating permittivity. Maxwell's equations are then solved with an extra

source term due to the fluctuating part of the permittivity. The permittivity function is described by the magnitude of the fluctuations, as well as by vertical and horizontal correlation functions. By using different values for different layers, this modeling approach has been used to model the returns from vegetation [Borgeaud et al., 1987] and layers of ice and snow [Tsang et al., 1985]. While the random medium approach usually requires fewer input parameters than the other two approaches, it is often not clear how the correlation functions of permittivity fluctuations are related to the physical medium parameters. Both the radiative transfer and random medium approaches do not readily provide physical insight about the scattering processes responsible for the observed scattering behavior.

The discrete scatterer approach has been used to construct fairly simple models to predict the full polarimetric scattering from vegetation layers. The main advantage of this approach is that it requires relatively few calculations, and provides physical insight into the scattering processes responsible for the observed polarization signature. Since the full polarimetric scattering is predicted for each scattering mechanism included in the model, techniques such as the one described by Ioannidis and Hammers [1979] could be used to choose the optimum polarization that would enhance scattering from say the trunks in forested areas relative to that from say the branches. This may simplify the problem of estimating woody biomass in vegetated areas. This approach has been used successfully to model the observed polarimetric scattering by forested areas [Durden et al., 1989].

5.2 Implementation of Imaging Radar

a. Flight Electronics

The first practical imaging radar polarimeter utilizing the full power of polarization synthesis was the NASA Jet Propulsion Laboratory CV990 airborne synthetic aperture radar system [Zebker et al., 1987]. This system was configured in the polarimetric mode from May through July, 1985. The system was unfortunately destroyed along with the aircraft in a fire during an aborted take-off attempt in July 1985. The CV990 radar operated at a wavelength of 24.5 cm (L-band) and with a 4-look resolution of about 10 m by 10 m. The output images represent areas roughly 10 km by 10 km in size. Data were acquired

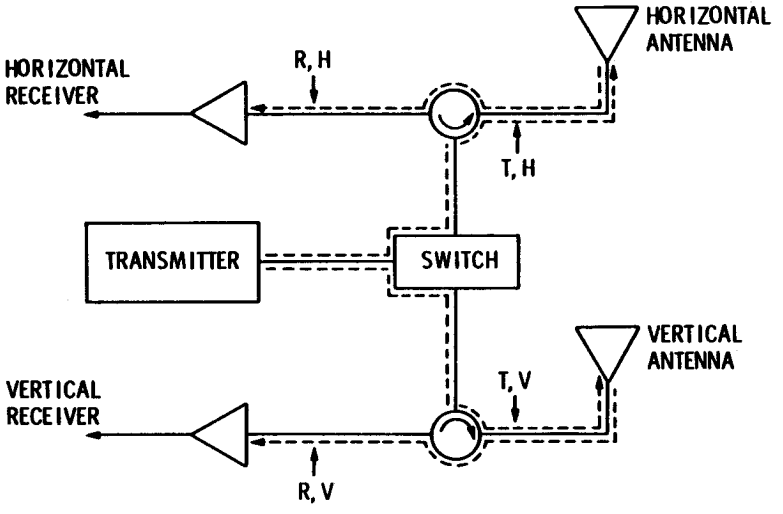

Figure 5.4 Block diagram showing the major components of the JPL CV990 SAR system. Also shown are the phase paths encountered by signals in the radar system. The path denoted t, h is the phase path of the horizontally polarized transmit signal, and so forth. These paths are measured from the received signals and compensated for in the data processor.

over a variety of sites throughout the United States (see Thompson [1986] for a description of all available data.)

A system block diagram of the CV990 imaging radar polarimeter is shown in Fig. 5.4. The four scattering matrix elements were measured by first transmitting a pulse through the horizontally polarized feed of the antenna and subsequently receiving signals simultaneously on both feeds. The next transmit event utilizes the vertically polarized antenna feed for transmit, followed again by simultaneous recording from both antenna ports. This approach is shown schematically in Fig. 5.5. With this implementation, each horizontally polarized transmit pulse and each vertically polarized transmit pulse is offset in time from the other by half the interpulse period, typically 0.5 – 1 ms. In the data processor, a synthetic aperture is formed by coherently integrating many pulses; however, pulses corresponding to each different polarization combina-

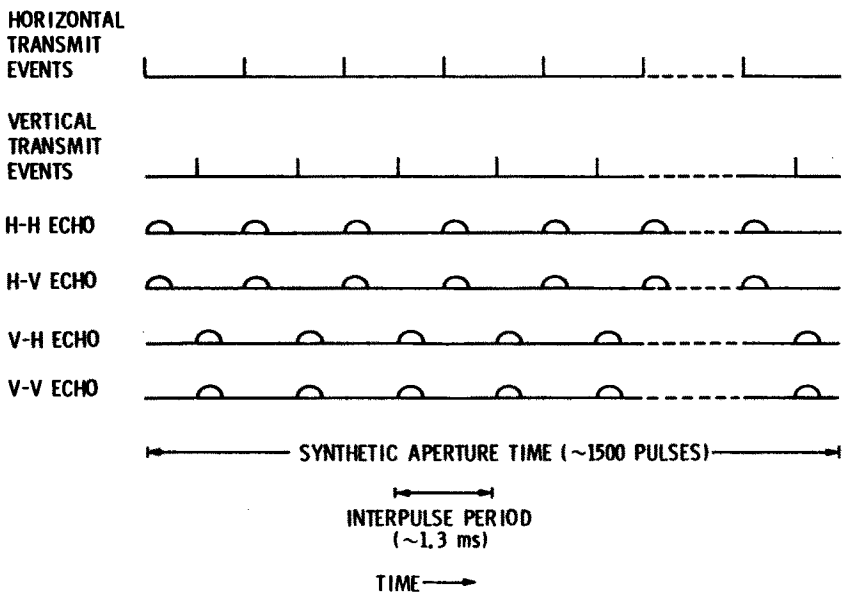

Figure 5.5 Near simultaneity is achieved from overlapping sets of pulses. Each horizontally polarized transmit pulse and each vertically polarized transmit pulse is offset in time from the other by half the interpulse period, typically 0.5 – 1 ms. In the data processor, a synthetic aperture is formed by coherently integrating many pulses; however, pulses corresponding to each different polarization combination are isolated and integrated independently from the other pulses. The total coherent integration required to achieve 3 m single-look resolution consists of approximately 1500 pulses over a 2 second period; therefore the interspersed sets of pulses correspond to very nearly the same synthesized spatial array.

tion are isolated and integrated independently from the other pulses. The total coherent integration required to achieve 3-m single-look resolution consists of approximately 1500 pulses over a 2 second period; therefore the interspersed sets of pulses correspond to very nearly the same synthesized spatial array.

The major effect of the nonexact simultaneity in each synthesized spatial array is the decorrelation of the four, independent, integrated signals as the integration limits are varied to correspond to each of the four synthetic apertures. Decorrelation results from the spatial coherence properties of the surface – each patch on the surface must be viewed from nearly the same direction or else the signals are unrelated.

This is the so-called "speckle" effect. In the aircraft implementations discussed here, this effect is of little consequence as the pulse repetition rate is large compared to the change in viewing angle from platform velocity. Consequently the reduction of intensity from decorrelation in our system for a shift of one interpulse period time out of a coherent integration of 1500 pulses is negligible compared to the total measured intensity, and we can consider to a good approximation that the processed signals arise from the synthesized arrays identical in spatial position.

Several additional polarimetric imaging systems have since been developed or are currently under development. The Jet Propulsion Laboratory is currently operating the successor to the CV990 polarimeter, a new system operating at three wavelengths (6 cm, 24 cm, and 68 cm) simultaneously. This instrument is installed on a DC-8 aircraft based at Ames Research Center in Mountain View, California. All three polarimeters on the DC-8 have similar resolution and image parameters to the CV990 radar. This system, which became operational in Spring 1988, collected data over many types of terrain, including lava fields, forests, agricultural areas, ice regions, and the open ocean.

The Environmental Research Institute of Michigan has also tested a new airborne imaging polarimeter [Kozma et al., 1986]. This instrument operates at three wavelengths, 3 cm, 6 cm, and 24 cm (X-, C-, and L-band) at a slightly higher resolution than the JPL instrument, 1.6 or 3.2 m in range resolution and 2.2 m single-look in azimuth (The JPL single look resolution is 3.2 m.) The platform for the ERIM radar is a P-3 aircraft. This system also measures the complex scattering matrix [S] for each single look resolution element in a scene of swath width 6 km or 12 km. We note that both this system and the above-mentioned JPL system can image swaths greater than 20 km in width, however data rate limitations preclude polarimetric data acquisition in this mode.

Another airborne polarimetric radar is the Canadian Centre for Remote Sensing CV580 radar [Goodenough and Livingstone, 1985]. This is an improved version of an ERIM SAR that CCRS operated from 1981–1984. The current system consists of a 6 cm wavelength radar and is being augmented with a 3 cm wavelength radar. Both of these radars now employ digital data recording, which is required for subsequent polarization synthesis.

The next step in technology development for polarimetric radar

systems is the implementation of a spaceborne unit, providing wide swaths and global imaging capabilities. The first of this new class of polarimeter will be the NASA Shuttle Imaging Radar C (SIR-C), now scheduled for launch in 1991. This unit will have dual wavelength (24 cm and 6 cm) polarimetric capability. An X-band system, built by a German and Italian team, will be flown simultaneously but will not have polarimetric capability. Data will be acquired over sites distributed around the world on two space shuttle flights. The signals will be recorded on-board the shuttle on digital tape and will be processed on the ground to produce the polarimetric data sets.

The SIR-C radar forms the basis of a prototype for the next in NASA's continuing remote sensing program, a radar designed to fly on the Earth Observing System satellite, now scheduled for launch in the late 1990's. This will be a free-flying satellite dedicated to continual long-term monitoring of the Earth's surface. Although exact wavelengths and modes remain to be defined, multi-wavelength polarimetry is one of the areas of highest interest for the investigators.

b. Data Processing

Early synthetic aperture radar systems were designed with much higher data rates than could be reasonably accommodated by existing computers, therefore the image products were typically produced by optical processors. Sets of lenses and film provided the needed Fourier transform and convolution operations to convert the measured signals into high-resolution image products. Optical techniques remained the only low-cost approach to data processing until the late 1970's, when digital data acquisition systems and computers became cheap and fast enough to be cost efficient.

The advent of the digital systems also made it possible to implement complex analysis procedures easily, including the ability to synthesize polarizations from the measured scattering or Stokes matrix elements. It is much more cumbersome to measure the phase of signals in the optical processors, particularly when the fields to be compared are not measured exactly simultaneously, which is the situation encountered in any of the polarimetric radars described above.

We can illustrate modern (1989) radar processing by describing the JPL DC-8 P, L, and C-band radar data processor. The signals from the four polarization channels (hh, hv, vh, vv) are each sampled at a 45 MHz rate and stored on high-density digital tapes. Each tape holds

roughly 15 minutes of data from each of the three radars at all four channels. The total volume of data on a tape is about 72 Gbits. Clearly not all of this data may be processed at one time by the computer, therefore on the ground a small portion (4 Gbits) is transferred to the disk storage system for further processing. This corresponds to a 10 by 10 km fully polarimetric frame at each frequency.

The data processor reads this data and compresses in the range direction by a frequency domain convolution with the range modulation function. The data are next pre-summed by a factor of four to further reduce data volume. The pre-summing operation must be implemented after the range compression as the processor must operate at non-zero squint angles because the antennas on the airplane are body fixed and not gimbaled. After presumming, the data set for each polarization channel and each frequency is Fourier transformed in the azimuth direction. Here the signal may be interpolated along the curves of the range history for targets at each desired output range – the "range migration correction." Finally the interpolated data set is multiplied by the proper azimuth reference function and inverse transformed to produce the complex high-resolution images for each of the canonical polarization channels.

c. Phase calibration

Phase calibration is the next required step in utilization of imaging radar polarimeter data, as errors in the phase relationship between polarization channels result in incorrect synthesis of polarization states, and may lead to false conclusions about the nature of scatterers on the surface. The Stokes matrices measured by an imaging radar polarimeter provide in themselves adequate information for accurate phase calibration of the observed polarimetric characteristics of a surface. This property allows the data to be reduced in volume in an operational synthetic aperture radar correlator with no prior knowledge of the conditions at the surface. No ground calibration equipment is necessary as all important parameters are derived from the data themselves.

Using the same system model as Zebker et al., [1987], we illustrate the signal phase paths in Fig. 5.5. If the true scattering matrix for a resolution element [S] is given by

$$[\mathbf{S}] = \begin{pmatrix} S_{hh} & S_{hv} \\ S_{vh} & S_{vv} \end{pmatrix} \tag{15}$$

where S_{ij} refers to the complex scattering amplitude for j-transmit,

i-receive polarization, due to the as yet uncorrected path differences in the radar hardware, what we actually measure is instead a receive matrix [R]:

$$[\mathbf{R}] = \begin{pmatrix} S_{hh} \exp\, j(\phi_{t,h} + \phi_{r,h}) & S_{hv} \exp\, j(\phi_{t,v} + \phi_{r,h}) \\ S_{vh} \exp\, j(\phi_{t,h} + \phi_{r,v}) & S_{vv} \exp\, j(\phi_{t,v} + \phi_{r,v}) \end{pmatrix} \tag{16}$$

where the phase factors correspond to the paths shown in Fig. 5.5. For notational simplicity we can factor out the phase on the vv term, resulting in

$$[\mathbf{R}] = \exp\, j(\phi_{t,v} + \phi_{r,v}) \begin{pmatrix} S_{hh} \exp\, j(\phi_t + \phi_r) & S_{hv} \exp\, j\phi_r \\ S_{vh} \exp\, j\phi_t & S_{vv} \end{pmatrix} \tag{17}$$

where $\phi_t = \phi_{t,h} - \phi_{t,v}$ and $\phi_r = \phi_{r,h} - \phi_{r,v}$.

Now, in the backscatter case, reciprocity dictates that $S_{hv} = S_{vh}$, thus we can solve for the difference $\phi_t - \phi_r$ by examining the complex product $R_{hv}R_{vh}^* = S_{hv}S_{vh}^* \exp\, j(\phi_t - \phi_r)$ averaged over the image. For each pixel the argument of this product will vary slightly as the system noise in each of the channels is uncorrelated, but we may average over many pixels to obtain the mean value which depends mainly on the phase path difference we are interested in.

Finally, if we know the dominant scattering mechanism at at least one point in the image, we can determine the rest of the factors necessary for phase calibration. Typically, a looser constraint is required; knowledge of the predicted phase difference of the hh and vv signals suffices for determination of $\phi_t + \phi_r$. These two sum and difference equations may now be solved for the individual phases ϕ_t and ϕ_r. These factors relate the measured matrix [R] to [S] which we may determine from

$$\mathbf{S} = \begin{pmatrix} R_{hh} \exp\, -j(\phi_t + \phi_r) & R_{hv} \exp\,(-j\phi_r) \\ R_{vh} \exp\,(-j\phi_t) & R_{vv} \end{pmatrix} \tag{18}$$

Note that this determination omits the leading phase factor of equation (3), as only the relative phases are preserved.

The Stokes matrices, rather than saving the individual scattering matrices, may also be used in the phase calibration procedure. This step is important as it allows averaging ("looks") of the radar data prior to distribution, which makes feasible many more applications of polarimetric radar data. We can ignore the leading factor $\exp\, j(\phi_{t,v} +$

$\phi_{r,v}$) in equation (17) above as calculation of the Stokes matrix removes this term – the Stokes matrix elements are defined only in terms of the relative phases of the polarimetric channels (see (12)). The first step in data volume reduction is the symmetrization of the scattering matrices. We repeat the estimation of $R_{hv}R_{vh}^*$ as above, and store the value of the average phase difference over the full image in a header which accompanies the data set. We then apply equation (17) and obtain a scattering matrix for each pixel in which the off-diagonal elements possess the same phase factor. Since the off-diagonal elements are now in phase, they may be averaged without introducing errors. We thus modify **R** to get a new matrix [**Z**]

$$[\mathbf{Z}] = \begin{pmatrix} S_{hh} \exp j(\phi_t + \phi_r) & S_{hv} \exp j\phi_r \\ S_{vh} \exp(j\phi_t) \exp[-j(\phi_t - \phi_r)] & S_{vv} \end{pmatrix} \tag{19a}$$

or

$$[\mathbf{Z}] = \begin{pmatrix} S_{hh} \exp j(\phi_t + \phi_r) & S_{hv} \exp j\phi_r \\ S_{vh} \exp j\phi_r & S_{vv} \end{pmatrix} \tag{19b}$$

We next obtain the symmetric matrix [**Y**] from symmetrizing [**Z**]:

$$[\mathbf{Y}] = \frac{1}{2}([\mathbf{Z}] + [\tilde{\mathbf{Z}}]) \tag{20}$$

Knowledge of [**Y**] allows us to calculate the Stokes matrix elements using (12). The values of [**Y**] and [**S**] do not yet agree because the data have not yet been phase calibrated, which must be accomplished in order to decode the polarizations correctly. These elements of [**Y**] are the data values which are produced by the standard data processor, before phase calibration:

$$Y_{hh}Y_{hh}^* = S_{hh}S_{hh}^* \tag{21a}$$
$$Y_{vv}Y_{vv}^* = S_{vv}S_{vv}^* \tag{21b}$$
$$Y_{hv}Y_{hv}^* = S_{hv}S_{hv}^* \tag{21c}$$
$$Y_{hh}Y_{vv}^* = S_{hh}S_{vv}^* \exp j(\phi_t + \phi_r) \tag{21d}$$
$$Y_{hh}Y_{hv}^* = S_{hh}S_{hv}^* \exp j\phi_t \tag{21e}$$
$$Y_{vh}Y_{vv}^* = S_{vh}S_{vv}^* \exp j\phi_r \tag{21f}$$

We again must select an area in the image for which the scattering phase difference between *hh* and *vv* is known; it is usually chosen from an area where the phase difference theoretically is near zero. As

discussed in Zebker et al., [1987], this yields an estimate of the sum $\phi_t + \phi_r$. Recall that we previously saved the value $\phi_t - \phi_r$ in the header of the data file; these two equations in two unknowns are solved for the individual values.

Thus, what remains is to apply the newly derived phases ϕ_t and ϕ_r to the stored Stokes matrices. This results in phase calibrated matrix cross-products (denoted in relation to a scattering matrix [O]) related to those of [Y] by:

$$O_{hh}O_{hh}^* = Y_{hh}Y_{hh}^* \tag{22a}$$
$$O_{vv}O_{vv}^* = Y_{vv}Y_{vv}^* \tag{22b}$$
$$O_{hv}O_{hv}^* = Y_{hv}Y_{hv}^* \tag{22c}$$
$$O_{hh}O_{vv}^* = Y_{hh}Y_{vv}^* \exp\left[-j(\phi_t + \phi_r)\right] \tag{22d}$$
$$O_{hh}O_{hv}^* = Y_{hh}Y_{hv}^* \exp\left(-j\phi_t\right) \tag{22e}$$
$$O_{vh}O_{vv}^* = Y_{vh}Y_{vv}^* \exp\left(-j\phi_r\right) \tag{22f}$$

Note that these cross-products correspond to the correctly phase calibrated Stokes matrix (compare with (21) above), as the cross-products associated with [O] accurately depict the original scattering matrix elements with no auxiliary phase factors.

We note that formally there is an ambiguity in determining ϕ_t and ϕ_r from the two equations as each of the sum and difference may only be measured modulo 2π. Thus, ϕ_t and ϕ_r may each possess errors of π, that is, each may be the negative of the true value. The effect of this in practical situations is minimal, as it merely causes the component of radiation linearly polarized at 45° to be interpreted as polarized at 135°, and the reverse. For azimuthally isotropic scatterers, then, no change would be observed – this is the case for most natural surfaces. However, for applications in which the distinction between 45° and 135° is important this possible ambiguity must be noted.

d. Data compression

The volume of data produced by the DC-8 data processor in the form of the high resolution complex images is 372 Mbytes for a three frequency fully polarimetric image. For practical uses this must be reduced further, hence a data compression scheme is employed which results in a 30 Mbyte data set. Consider a symmetrical Stokes matrix [M] of the form given in (12). As pointed out before, [M] may contain up to nine independent real numbers. Conventional computer storage

would require 36 bytes to store these numbers on disk or tape, nine distinct floating point values of four bytes each. At present JPL uses a quantization technique whereby those 36 bytes may be reduced to only ten. In addition, the data are further reduced to four-look format, yielding an additional factor of four improvement.

The compression procedure is implemented as follows. Each data set is scaled by a single value for all pixels such that the dynamic range of the total power elements in the Stokes matrices (the M_{11} element) falls within values between 2^{-128} and 2^{127}. Since radar images typically exhibit less than 30 dB dymanic range this condition is easily met. The total power for each matrix is then coded into two bytes, one for the exponent in the above range and one for mantissa. The remaining eight elements are then normalized to the M_{11} element in the Stokes matrix.

Four of these elements (those related to the cross products of co- and cross-polarized channels) are observationally found to be much smaller than M_{11}; many theories predict these elements to be small or zero for most natural surfaces. Therefore, before encoding, the square root of each of the four, normalized still by M_{11}, is calculated. Each of the eight values is next truncated to eight bits (one byte) and the resulting eight bytes are saved. These eight bytes plus the two for the total power are then stored, requiring only 10 bytes per pixel.

The equations for the compression and decompression operations are given here for reference. For data encoding from the Stokes matrix to the compressed 10 byte format, the following apply:

$$\text{byte}(1) = \text{Int}\left(\frac{\log M_{11}}{\log 2}\right) \tag{23}$$

where $Int()$ is the integer part of.

$$\text{byte}(2) = \text{Int}\left[254 \cdot \left(\frac{M_{11}}{2^{\text{byte}(1)}} - 1.5\right)\right] \tag{24}$$

We then compute a normalization factor x, approximately equal to M_{11}. Choosing this factor for normalization results in slightly smaller errors than using M_{11} directly.

$$x = \left(\frac{\text{byte}(2)}{254} + 1.5\right) \cdot 2^{\text{byte}(1)} \tag{25}$$

The remaining eight bytes are coded as follows:

$$\text{byte}(3) = 127 \cdot M_{12}/x \tag{26a}$$

$$\text{byte}(4) = 127 \cdot \text{sign}(M_{13}/x) \cdot \sqrt{|M_{13}/x|} \tag{26b}$$

$$\text{byte}(5) = 127 \cdot \text{sign}(M_{14}/x) \cdot \sqrt{|M_{14}/x|} \tag{26c}$$

$$\text{byte}(6) = 127 \cdot \text{sign}(M_{23}/x) \cdot \sqrt{|M_{23}/x|} \tag{26d}$$

$$\text{byte}(7) = 127 \cdot \text{sign}(M_{24}/x) \cdot \sqrt{|M_{24}/x|} \tag{26e}$$

$$\text{byte}(8) = 127 \cdot M_{33}/x \tag{26f}$$

$$\text{byte}(9) = 127 \cdot M_{34}/x \tag{26g}$$

$$\text{byte}(10) = 127 \cdot M_{44}/x \tag{26h}$$

To reconstruct the Stokes matrix from the reduced data the following operations are required:

$$M_{11} = \left(\frac{\text{byte}(2)}{254} + 1.5\right) \cdot 2^{\text{byte}(1)} \tag{27a}$$

$$M_{12} = \text{byte}(3) \cdot \frac{M_{11}}{127} \tag{27b}$$

$$M_{13} = \text{sign}(\text{byte}(4)) \cdot \left(\frac{\text{byte}(4)}{127}\right)^2 \cdot M_{11} \tag{27c}$$

$$M_{14} = \text{sign}(\text{byte}(5)) \cdot \left(\frac{\text{byte}(5)}{127}\right)^2 \cdot M_{11} \tag{27d}$$

$$M_{23} = \text{sign}(\text{byte}(6)) \cdot \left(\frac{\text{byte}(6)}{127}\right)^2 \cdot M_{11} \tag{27e}$$

$$M_{24} = \text{sign}(\text{byte}(7)) \cdot \left(\frac{\text{byte}(7)}{127}\right)^2 \cdot M_{11} \tag{27f}$$

$$M_{33} = \text{byte}(8) \cdot \frac{M_{11}}{127} \tag{27g}$$

$$M_{34} = \text{byte}(9) \cdot \frac{M_{11}}{127} \tag{27h}$$

$$M_{44} = \text{byte}(10) \cdot \frac{M_{11}}{127} \tag{27i}$$

$$M_{22} = M_{11} - M_{33} - M_{44} \tag{27j}$$

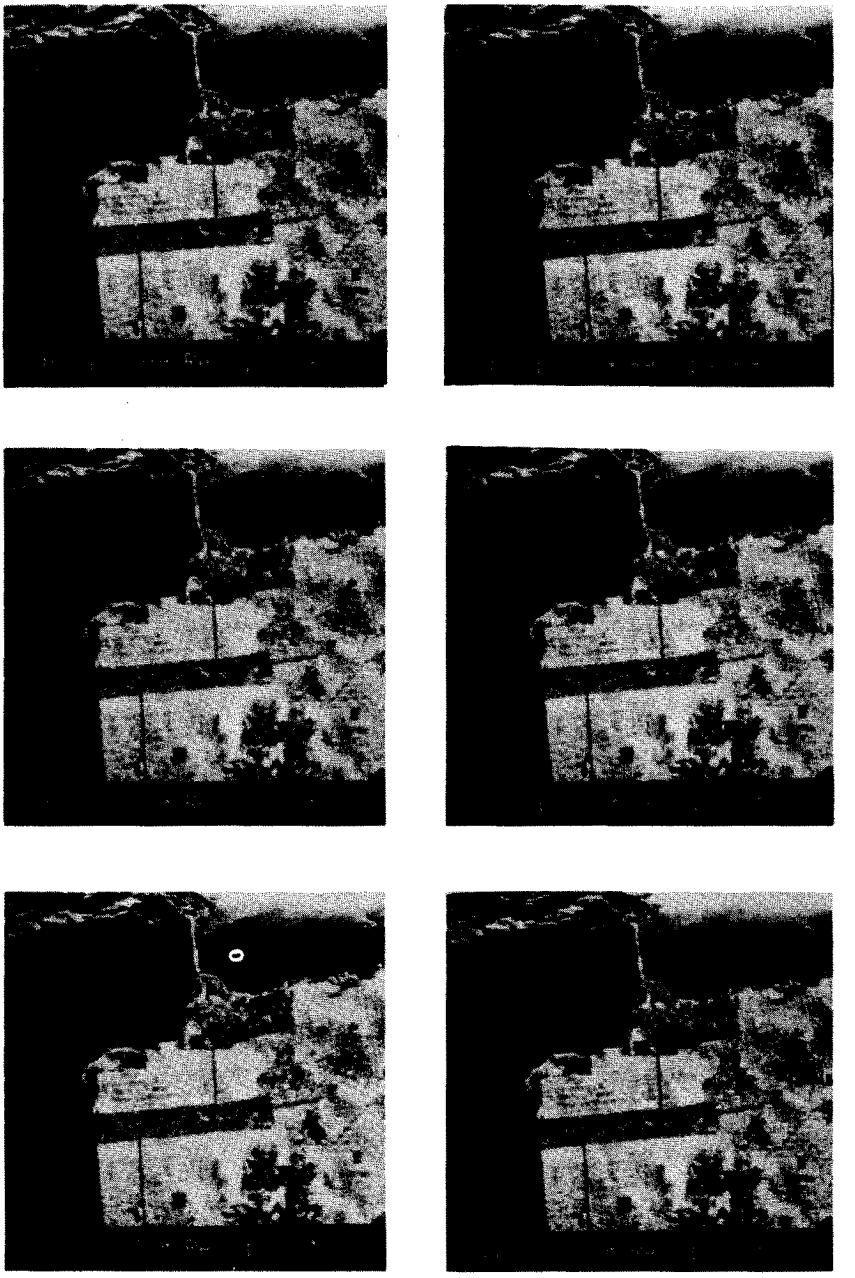

Figure 5.6 Continued

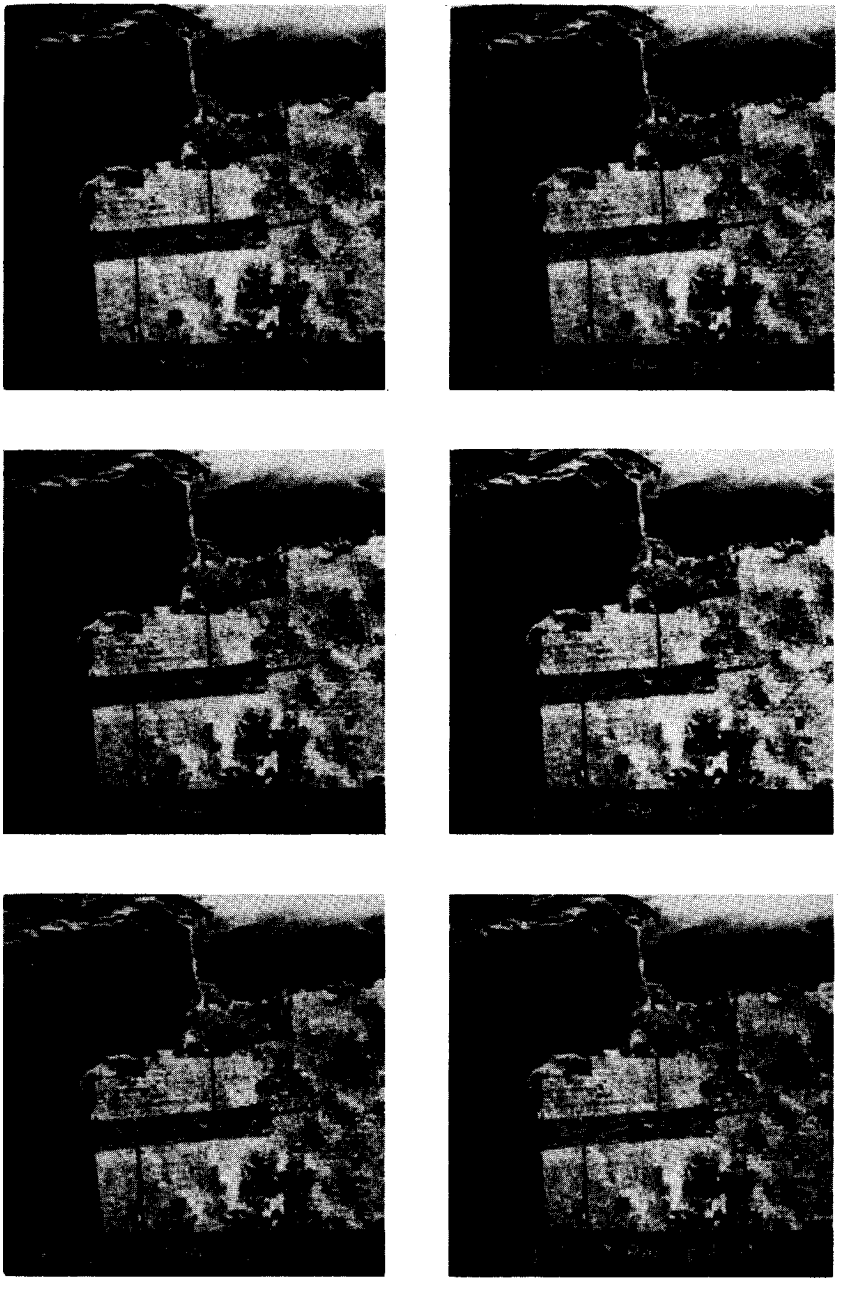

Figure 5.6 Continued

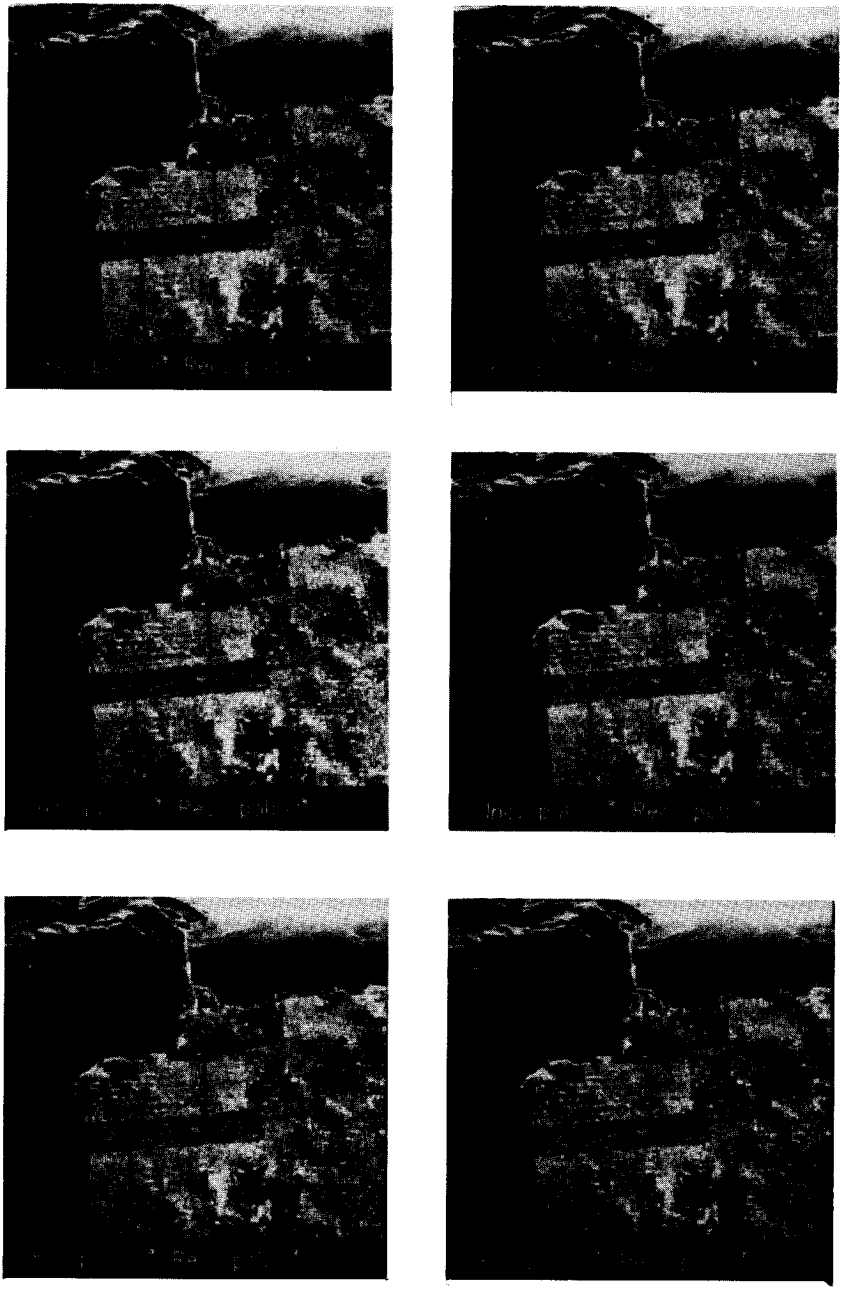

Figure 5.6 Continued

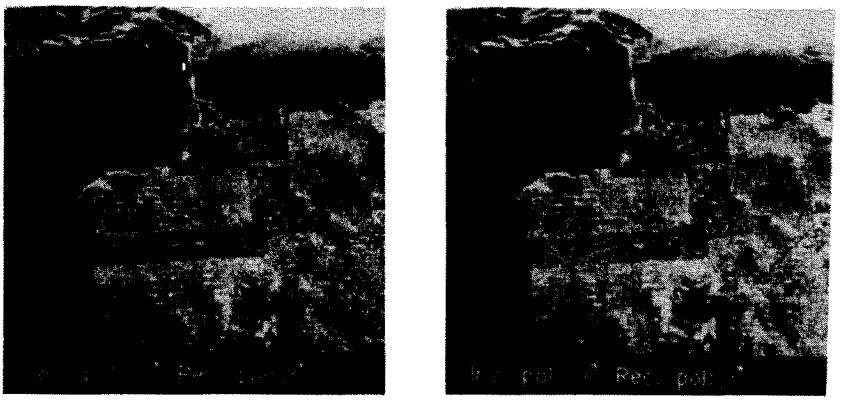

Figure 5.6 Results of synthesizing a set of linear, co-polarized antennas and applying them to data collected over San Francisco, California. This figure consists of twenty images; the first image corresponds to horizontally polarized antennas used for transmission and reception of signals. Scanning from left to right and from the first to the last image, the ellipse orientation angle of the linear polarization is advanced 2.5 degrees per image and the square root of the resulting scattering cross section is displayed. The last image thus corresponds to a linear polarization with an ellipse orientation angle of 47.5 degrees. For a complete discussion, see Zebker et al., [1987].

5.3 Observed Polarimetric Scattering Characteristics

Typical image products from the JPL CV990 polarimeter are discussed in detail by Zebker et al., [1987]. They present, for example, a figure consisting of 20 radar images, each at a slightly different synthesized linear polarization angle, varying from horizontal to linear at 47.5 degrees. This set of images is also shown in Fig. 5.6. These images yield evidence for different types of scattering occurring in different parts of the surface. This portion of San Francisco includes the Pacific Ocean, an urban portion of the city, and the vegetated Golden Gate Park. Here we only note that each area has its own variation of brightness with angle, for a complete discussion see Zebker et al., [1987].

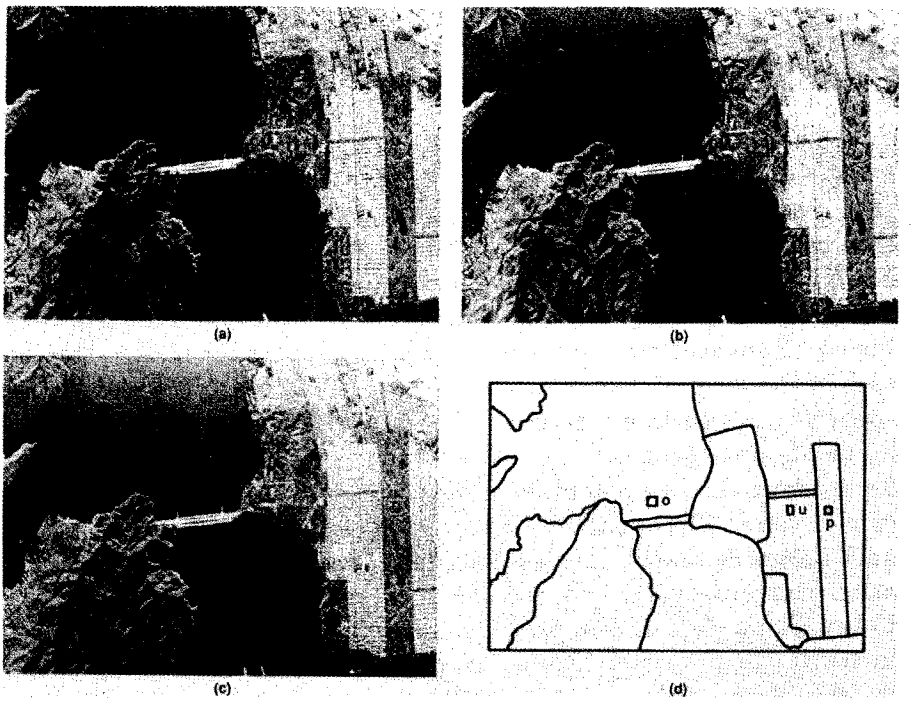

Figure 5.7 Total power images of San Francisco, California, obtained with the NASA/JPL DC-8 airborne SAR (a) P-band, (b) L-band, (c) C-band and (d) a location map for reference showing the locations of the extracted polarization signatures of the ocean (o), urban area (u) and park (p). The image covers an area of about 12 km by 5 km and each pixel represents approximately 12 m by 7 m on the ground. The radar illumination is from the top and the aircraft movement is from right to left.

In the rest of this section we shall discuss the observed multifrequency polarization signatures for a number of different earth terrain types. All the data were collected with the NASA/JPL imaging radar polarimeter during the spring and summer of 1988. The scenes presented include an image of the San Francisco area, a set of lava flows of varying roughness in the Mojave Desert (including Pisgah flow), a forested area near Mt. Shasta in California, and an image of sea ice in the Beaufort Sea. In each case we plot the polarization signatures at all three frequencies available on the DC-8 radar.

a. San Francisco

In Fig. 5.7 we show three total power (M_{11}) images of the San Francisco area, which include regions composed of ocean, urban development, city parks, and natural terrain. Figure 5.7(a) is the P-band data, 5.7(b) L-band, and 5.7(c) C-band. In Fig. 5.8 we show the associated co-polarized polarization signatures at each of the frequencies for the ocean, an urban area and an area in Golden Gate park. At each frequency the ocean area scatters in a manner consistent with Rice's small perturbation model (see above), the urban area scatters like a dihedral corner reflector, while the park scatters much more diffusely, that is, its signature possesses a large pedestal. This indicates the dominant scattering mechanisms responsible for the backscatter for each of the targets. The ocean scatter is predominantly single bounce, slightly rough surface scattering. The urban regions are characterized by two-bounce geometry as the incident waves are twice forward reflected from the face of a building to the ground and back to the radar, or vice versa. The apparent diffuse nature of the backscatter from the park indicates that in a vegetated area there exists considerable variation from pixel to pixel of the observed scattering properties, leading to the high pedestal. This variation may be due to a distinct variation in scattering properties among 10 m resolution elements, or perhaps to multiple scatter.

Thus, scattering mechanisms can be distinguished by examining the observed polarization signatures. While we have not yet described variations in frequency, the following examples will serve to illustrate that frequency effects may be used to further constrain the exact physical mechanisms important for radar backscatter.

b. Geology

In Figs. 5.9 and 5.10 we show the total power images and signatures obtained over the Pisgah lava flow in the Mojave desert in California. Plotted signatures correspond to part of the flow itself (a pahoehoe lava surface), an alluvial fan (medium roughness), and to the playa next to the flow (a very smooth surface). Comparing the signatures of the three surface types at a fixed frequency, we note that as the roughness of the surface increases, so does the observed pedestal height. This is quite consistent with the predictions of the slightly rough surface models, even though the surface r.m.s. heights exceed the strict range of validity of the model in the C-band case. If the signatures at the

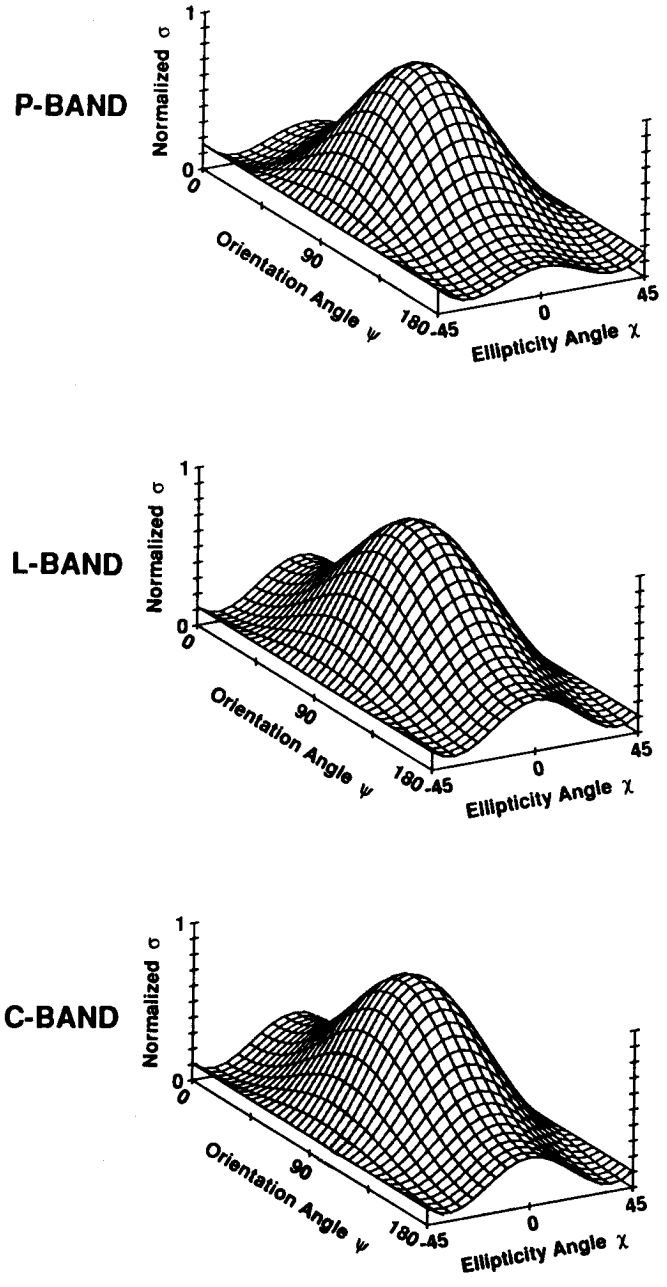

Figure 5.8 Continued

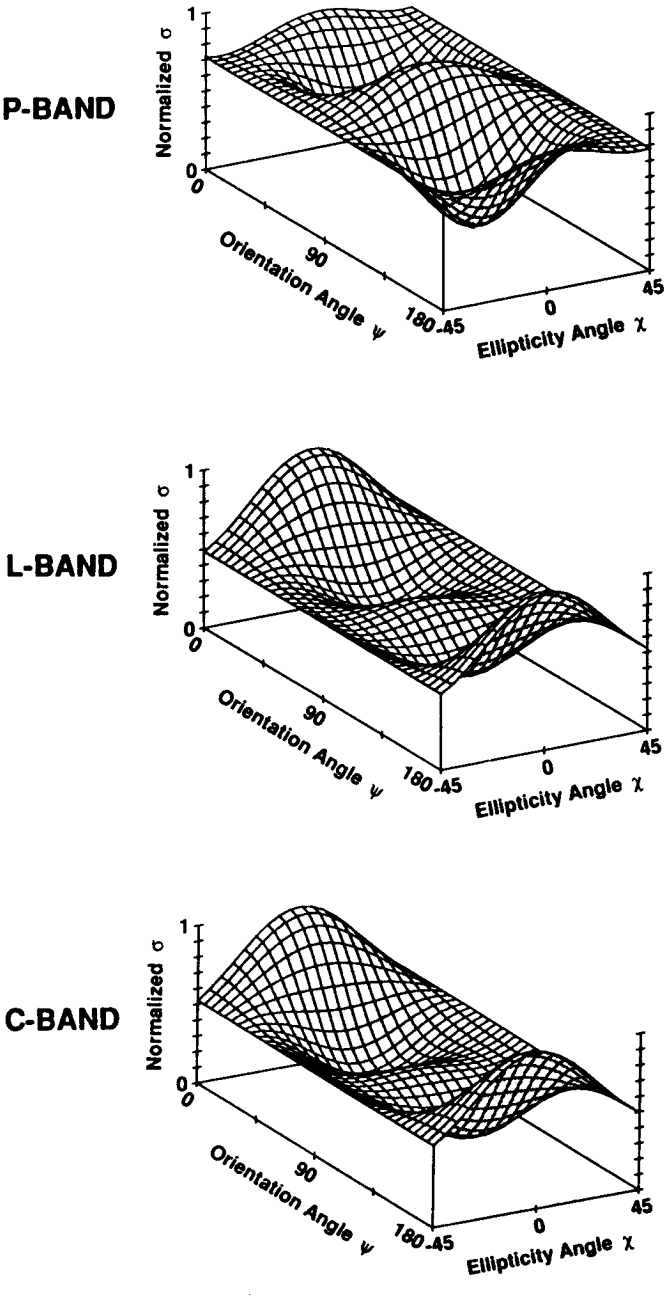

Figure 5.8 Continued

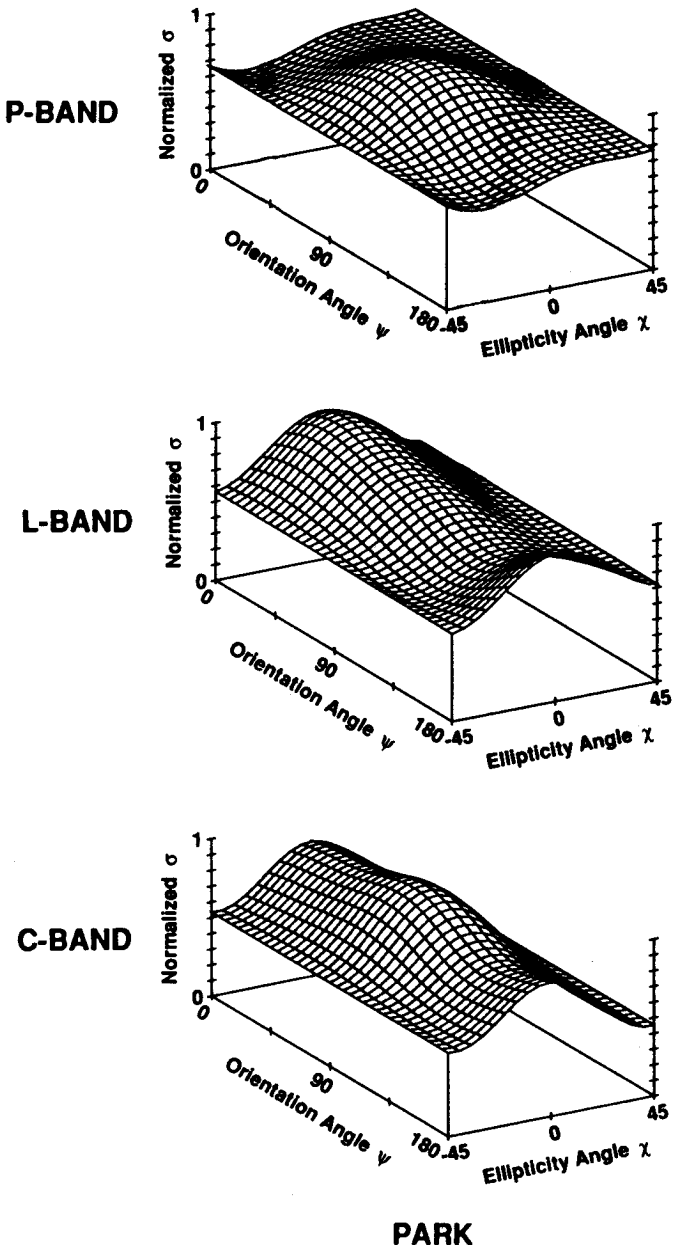

Figure 5.8 Three-frequency polarization signatures of the ocean (incidence angle = 43.8 degrees), an urban area (incidence angle = 44.6 degrees) and the park (incidence angle = 44.4 degrees) in the San Francisco image. Notice that all the signatures have distinctly different shapes, allowing one to infer that the ocean scattering is consistent with that predicted by slightly rough surface scattering models, while the urban scattering is dominated by double-reflections off the ground onto the sides of buildings before returning to the radar. The high pedestal observed in the park signals points to a high degree of variation in scattering properties from one pixel to the next for vegetated areas.

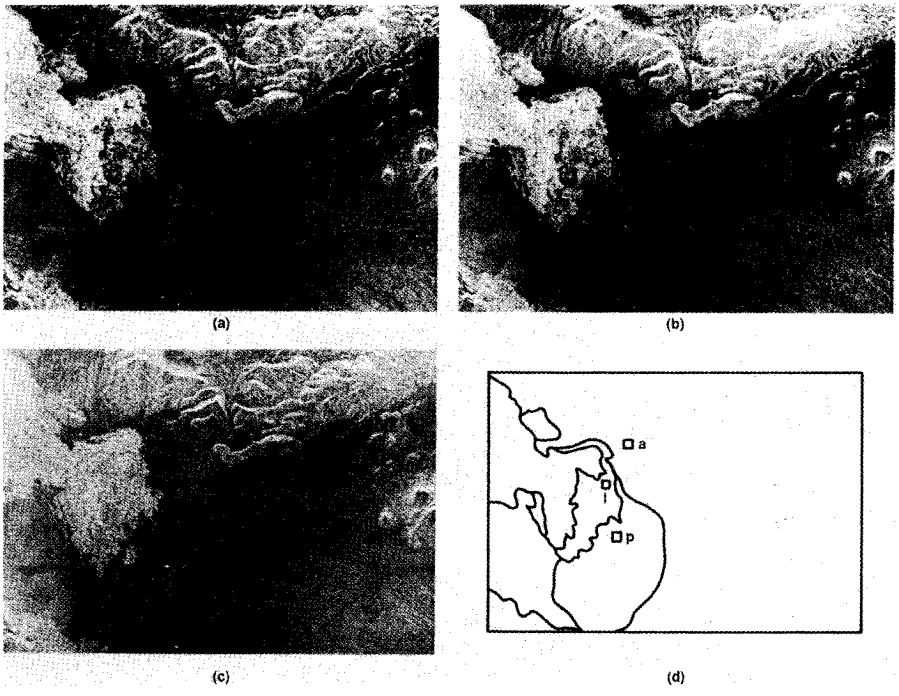

Figure 5.9 Total power images of the Pisgah lava flow area, California, obtained with the NASA/JPL DC-8 airborne SAR (a) P-band, (b) L-band, (c) C-band and (d) a location map for reference showing the locations of the extracted polarization signatures of the playa (p), alluvial surface (a) and pahoehoe lava (l). The image covers an area of about 12 km by 5 km and each pixel represents approximately 12 m by 7 m on the ground. The radar illumination is from the top and the aircraft movement is from right to left.

three frequencies are compared for the alluvial or pahoehoe surfaces, we see that the pedestal height increases with decreasing wavelength. This could be explained by the fact that for a fixed surface roughness, the surface "appears" rougher for the smaller wavelengths. The playa signatures show high pedestals at both P-band and C-band relative to that at L-band. While the change from L-band to C-band could be explained by the same argument as before, the P-band result may

be due to subsurface volume scattering due to the greater penetration capability of the P-band signals, or to a less favorable signal to noise ratio, or to a combination of both. At present, it is not possible to decide uniquely in favor of one possibility.

c. Vegetation

Figure 5.11 shows the total power images of a forested area near Mt. Shasta in California. Also noted in Fig. 5.11 are sample areas which are typical of heavy forest and clear-cut. In general we note that the contrast between the forested and clear-cut areas is greatest in the P-band image.

In Figure 5.12 we show polarization signatures for the heavily forested area and the clear-cut area. We note that, as in the case of the park in San Francisco, all the signatures appear to be composed of a variable portion sitting on top of a pedestal. The pedestal height varies with the type of scatterer, the heavy forest exhibiting a larger pedestal and the clear-cut a smaller pedestal. As discussed above, the pedestal is due to spatial variations in the observed scattering properties; we have interpreted this effect in terms of the presence of an unpolarized component (component with randomly varying polarization) in the spatially averaged return. In other words, the average return is partially polarized. When the pedestal height is zero, the average return is completely polarized, and variations in antenna polarization (receive or transmit) will cause relatively large variation in the average backscattered power. When the pedestal height is unity, i.e., the signature appears completely flat, the average return is completely unpolarized, and variation of antenna polarization will not change the average backscattered power. In general, the smaller the pedestal height, the greater the amount of polarized power in the average return, and hence, the more the average backscattered power will change with polarization.

The pedestal for the heavily forested area is large, indicating that a significant portion of the return is unpolarized. As mentioned above, this is related to a large variability in the observed scattering properties, suggesting that scattering from branches is important [Durden et al., 1989]. The clear-cut area has characteristics similar to the heavily forested area, except that the pedestal is lower.

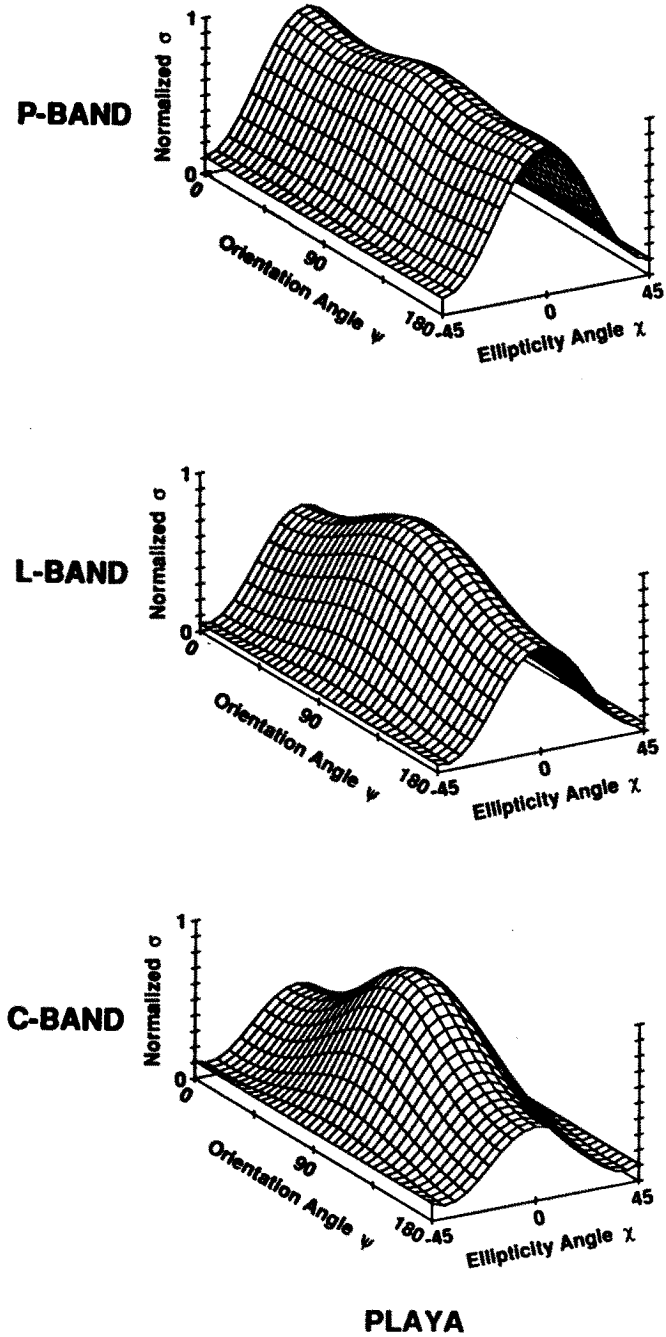

Figure 5.10 Continued

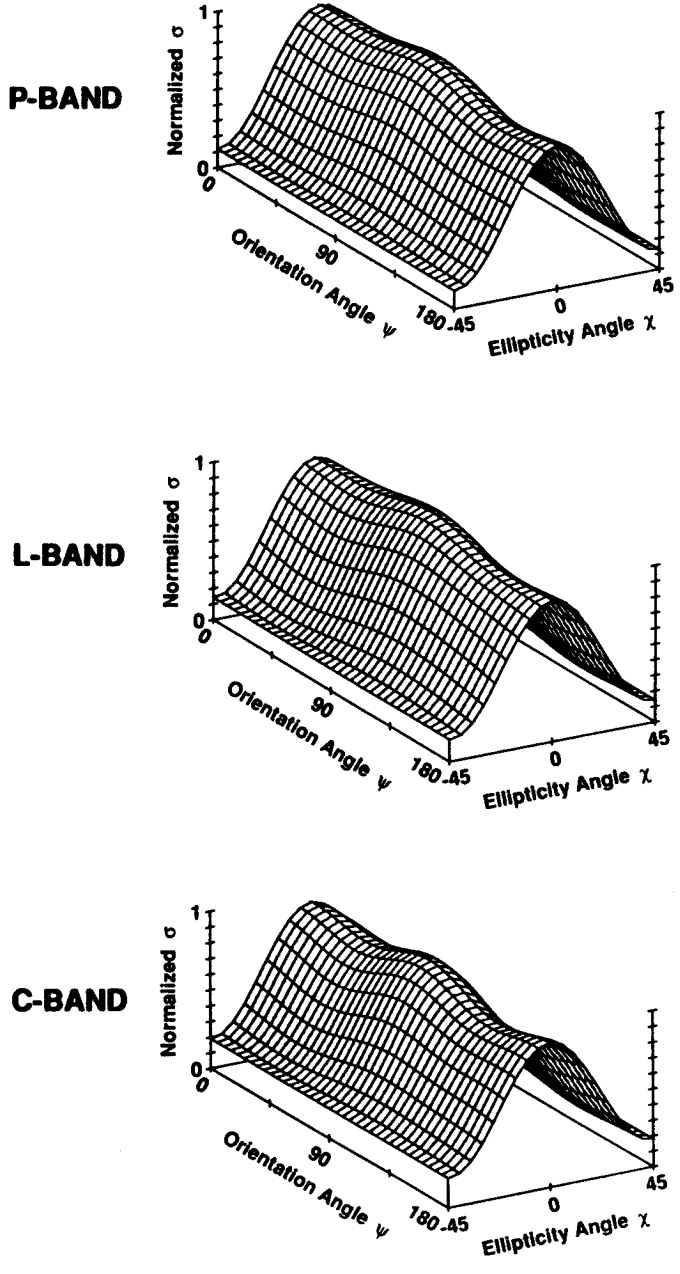

Figure 5.10 Continued

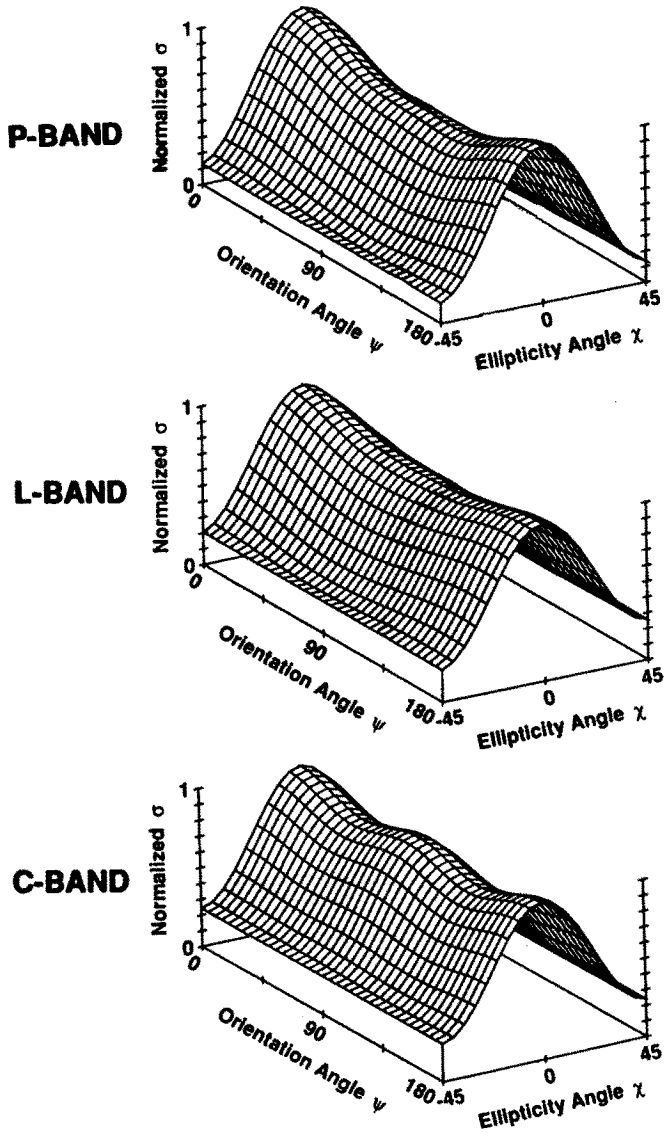

Figure 5.10 Three-frequency polarization signatures of the playa (incidence angle = 46.4 degrees, smooth surface, r.m.s. height less than 1 cm), the alluvial surface (incidence angle = 40.4 degrees, r.m.s. height approximately 2.5 cm) and the pahoehoe lava surface (incidence angle = 44 degrees, r.m.s. height approximately 4 cm) in the Pisgah lava flow image. Notice that the observed pedestal height increases with increasing surface roughness as well as with increasing frequency. We note here that even though all surfaces are strictly speaking too rough to apply the slightly rough surface model for interpretation of the C-band results, the observed trend is also predicted by the slightly rough surface model.

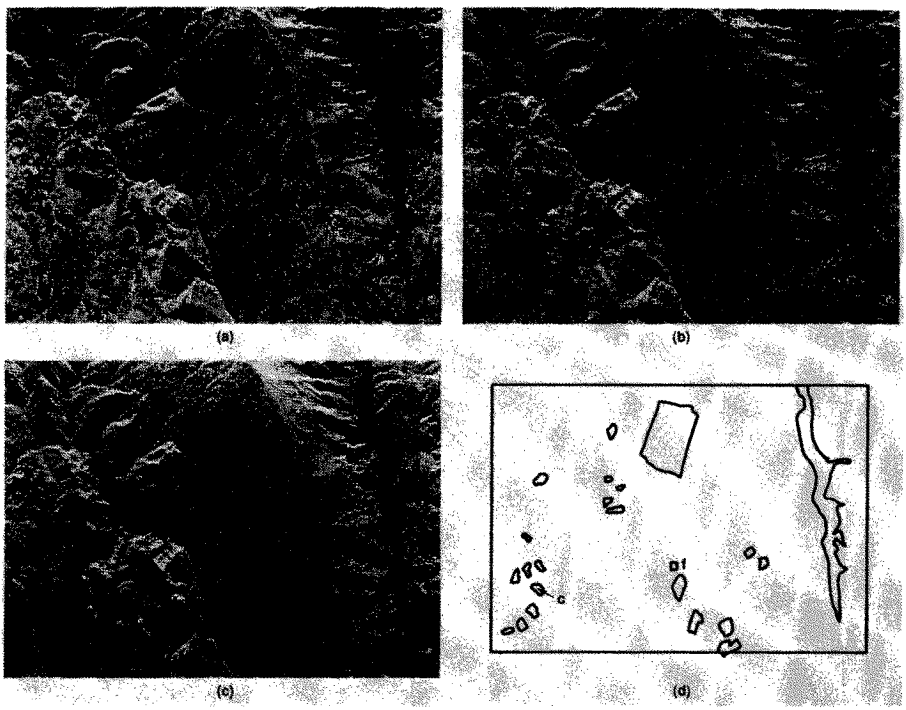

Figure 5.11 Total power images of Mount Shasta area, California, obtained with the NASA/JPL DC-8 airborne SAR (a) P-band, (b) L-band, (c) C-band and (d) a location map for reference showing the locations of the extracted polarization signatures of the forested area (f), and clear-cut (c). The image covers an area of about 12 km by 5 km and each pixel represents approximately 12 m by 7 m on the ground. The radar illumination is from the top and the aircraft movement is from right to left.

d. Sea Ice

Figures 5.13 and 5.14 illustrate the total power images and signatures, respectively, for both multi-year and first year ice in the Beaufort Sea off the coast of Alaska. First consider the total power images themselves. The C-band image is characterized by bright areas corresponding to the multi-year ice and dark regions corresponding to the first

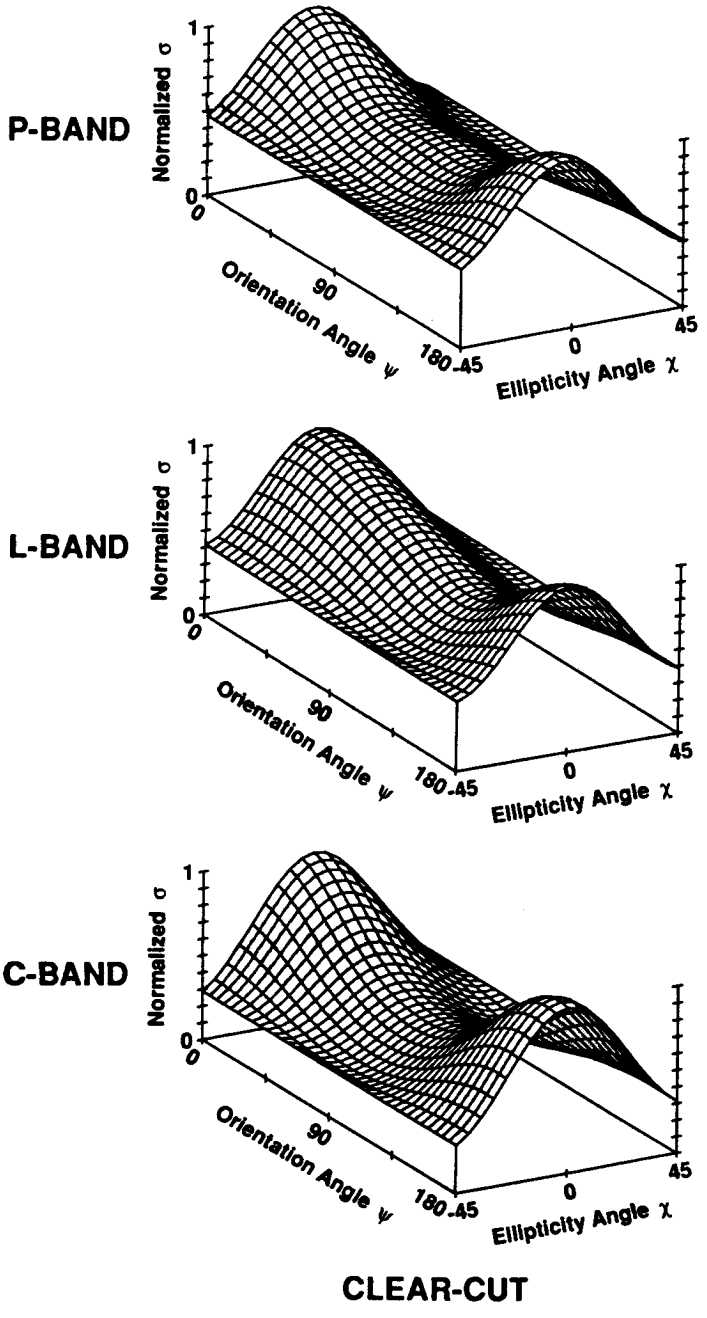

Figure 5.12. Continued

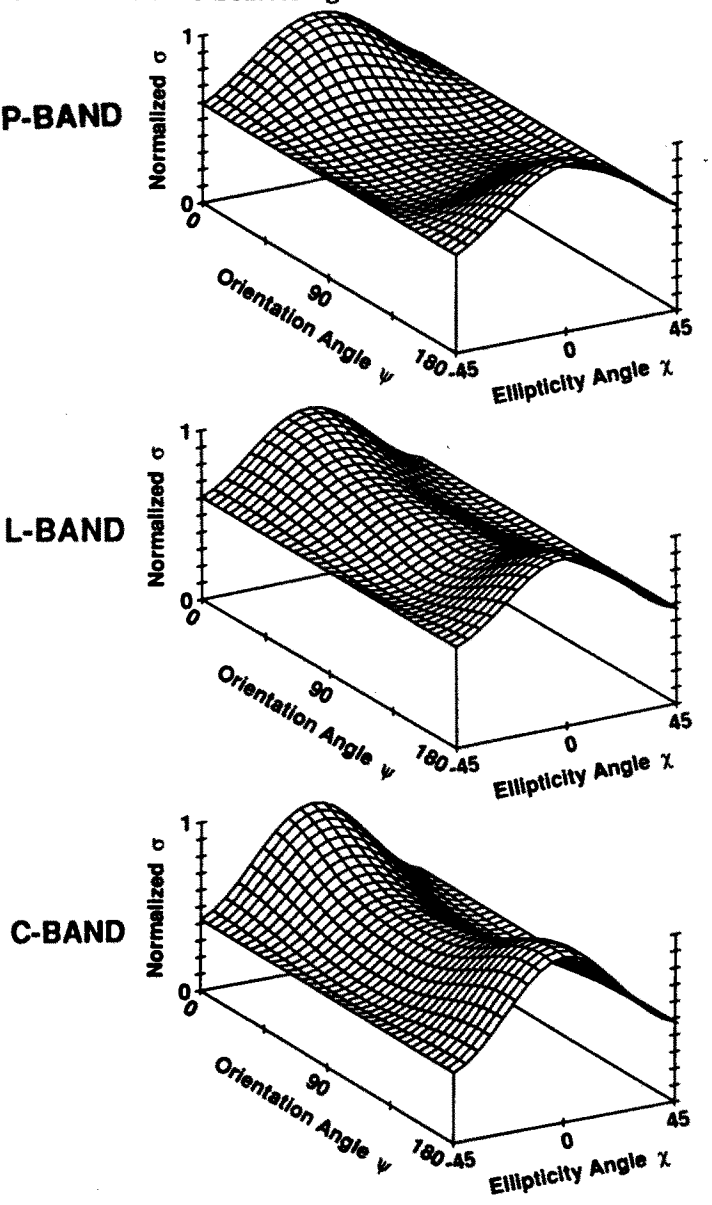

Figure 5.12 Three-frequency polarization signatures of a forested area (incidence angle = 52.9 degrees), and a clear-cut area (incidence angle = 50.6 degrees) in the Shasta image. Notice that all signatures have large pedestals, indicating a high degree of variation in scattering properties from one pixel to the next, suggesting that branch scattering is important [Durden et al., 1989] in the forested area.

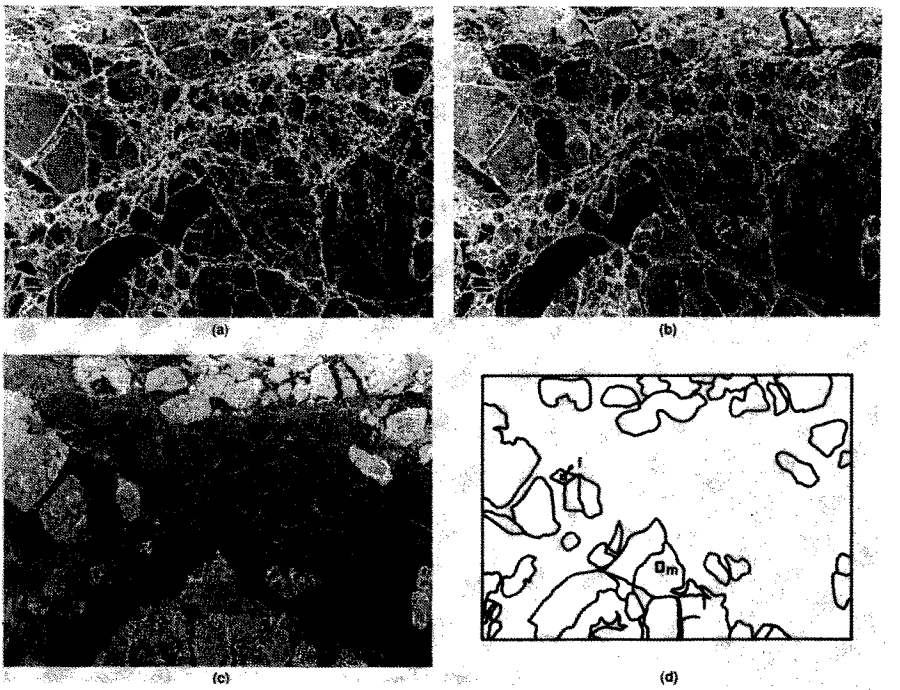

Figure 5.13 Total power images of sea ice in the Beaufort Sea, Alaska, obtained with the NASA/JPL DC-8 airborne SAR (a) P-band, (b) L-band, (c) C-band and (d) a location map for reference showing the locations of the extracted polarization signatures of the first year ice (f) and the multi-year ice (m). The image covers an area of about 12 km by 5 km and each pixel represents approximately 12 m by 7 m on the ground. The radar illumination is from the top and the aircraft movement is from right to left.

year ice. The P-band image, on the other hand, is dark for both the first and multi-year ice, but shows quite clearly the pressure ridges formed when the pieces of ice collide with each other. The L-band image exhibits intermediate behavior. When the polarimetric behavior of the scattering at the three frequencies is examined, the differences are even more striking. Note the pedestal height as a function of frequency for the multi-year ice — the P-band pedestal is quite small, while the C-

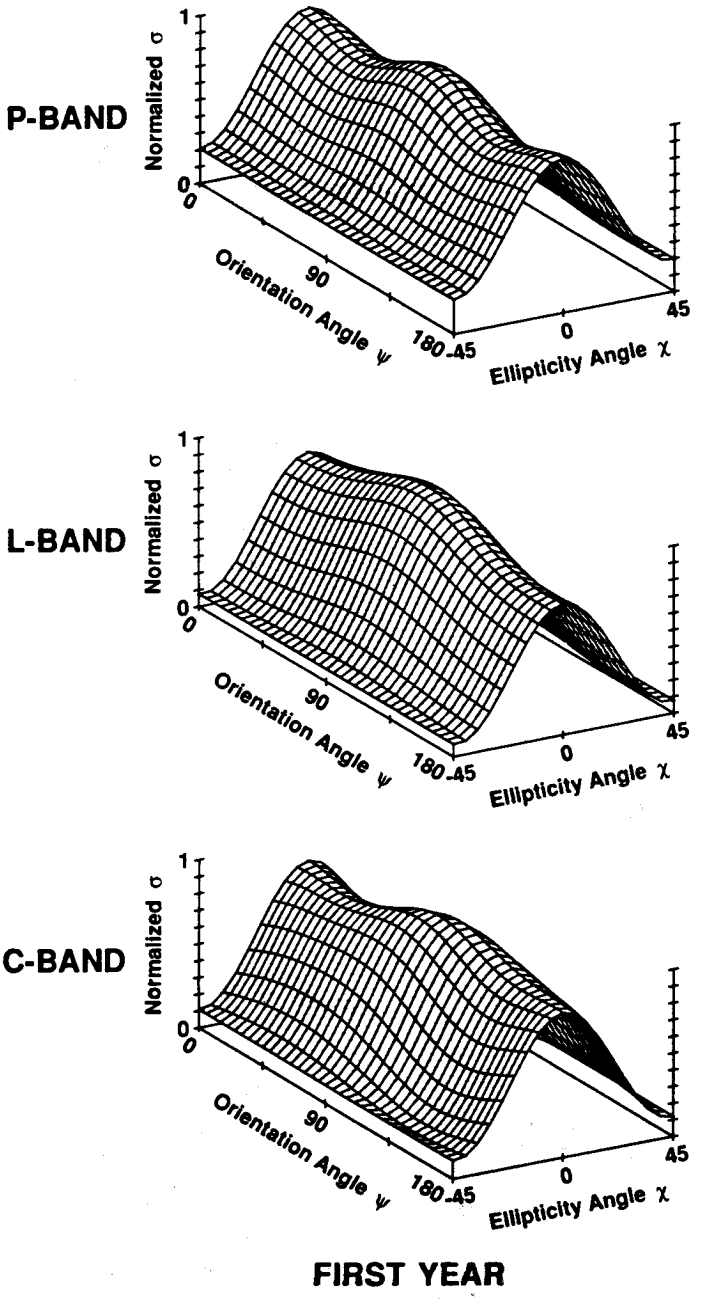

Figure 5.14 Continued

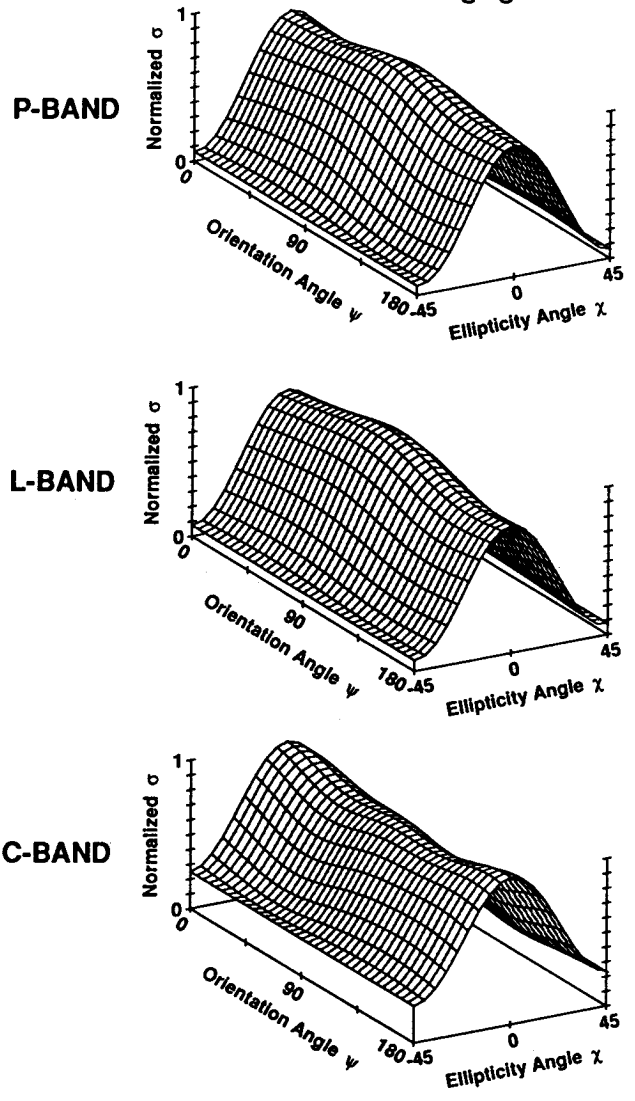

Figure 5.14 Three-frequency polarization signatures of first year ice (incidence angle = 36.2 degrees), and multi-year ice (incidence angle = 48.3 degrees) in the Beaufort Sea image. Note that for the first year ice, the pedestal decreases with increasing frequency. The opposite effect is observed for the multi-year ice, in which case the pedestal increases with increasing frequency. Two different models predict the observed behavior of the multi-year ice, but at present we do not have an explanation for the observed behavior of the first year ice.

band pedestal is the greatest of the three. For the first year ice, exactly the opposite behavior is seen. The P-band signature shows the highest and the C-band signature the lowest pedestal. One explanation for the multi-year ice behavior considers the ice to be formed of two layers, where the upper layer consists of randomly oriented oblong inclusions about the size of a C-band wavelength, several centimeters. The lower layer forms a solid, but slightly rough surface, or may consist of the underlying water. In this situation the C-band signal would interact strongly with the diffuse scattering upper layer, giving rise to the high pedestal. The longer wavelength L- and P-band signals would pass through the upper and be scattered by the lower layer, which is smooth enough to exhibit fairly polarized backscatter. Another explanation follows the same argument as that given for the signatures of the lava surface, where the ice is considered to be a dielectric half-space with a rough interface. The shorter the wavelength, the rougher the surface appears and the higher the resulting pedestal as predicted by the small perturbation model. At present we have no model to explain the first year ice behavior.

5.4 Summary

The basic theory underlying imaging radar polarimetry for the study of natural surfaces is fairly well developed at this point in time, that is, the fundamental equations are understood in the context of investigation of the Earth's surface. Several instruments are currently in operation with several others being planned, including spaceborne implementations. Techniques exist whereby polarimetric measurements of the Earth may be acquired, and data analysis procedures have been developed which render the data usable by scattering theorists and application-oriented investigators.

Conventional imaging radars operating with a single, fixed-polarization antenna are being supplanted by the next generation instrument capable of measuring the polarization of the scattered wave for any and all transmit polarizations. Already a wide variety of natural terrains have been mapped using these new instruments. The observed scattering characteristics vary as a function of polarization state and also of frequency. Nature appears to be described by what is now a bewildering variety of polarization signatures. At present we are un-

able to model accurately all of these types of scattering, but imaging polarimetry is a promising tool to aid in this process and in the understanding of the Earth system.

Acknowledgment

This work was performed at the Jet Propulsion Laboratory, California Institute of Technology, sponsored by the National Aeronautics and Space Administration. We would like to thank all the people involved in the JPL Radar Program who operated the imaging polarimeter and processed the data used in this manuscript.

References

[1] Agrawal, A. P., and W. M. Boerner, "Redevelopment of Kennaugh's target characteristic polarization state theory using the polarization transformation ratio for the coherent case," *IEEE Trans. Geoscience and Remote Sensing,* **GE-27**, 2–14, 1989.

[2] Boerner, W. M., "Use of polarization in electromagnetic inverse scattering," *Radio Science,* **16**, 1037–1045, 1981.

[3] Boerner, W. M., M. B. El-Arini, C. Y. Chan, and P. M. Mastoris, "Polarization dependence in electromagnetic inverse problems," *IEEE Trans. Antennas and Propagat.*, **AP-29**, 262–271, 1981.

[4] Boerner, W. M. et al., Ed., *Inverse Methods in Electromagnetic Scattering,* Reidel Publications, Hingham, MA, 1985.

[5] Boerner, W. M., B-Y. Foo, and H. J. Eom, "Interpretation of polarimetric copolarization phase term in the radar images obtained by the JPL airborne L-band SAR system," *IEEE Trans. Geoscience and Remote Sensing,* **GE-25**, 77–82, 1987.

[6] Bohnert, J. I., "Part IV - Measurement of elliptically polarized antennas," *Proceedings of the IRE,* **39**, 549–552, 1951.

[7] Borgeaud, M., R. T. Shin, and J. A. Kong, "Theoretical models for polarimetric radar clutter," *Journal of Electromagnetic Waves and Applications,* **1**, No. 1, 73–89, 1987.

[8] Born, M., and E. Wolf, *Principles of Optics*, Sixth Edition, 24-32, Pergamon Press, New York, 1980.

[9] Copeland, J. R., "Radar target classification by polarization properties," *Proceedings of the IRE,* **48**, 1290–1296, 1960.

[10] Deschamps, G. A., "Part II - Geometrical representation of the polarization of a plane magnetic wave," *Proceedings of the IRE,* **39**, 540–544, 1951.

[11] Durden, S. L., J. J. van Zyl and H. A. Zebker, "Modeling and observations of the radar polarization signatures of forested areas," *IEEE Trans. Geoscience and Remote Sensing,* **GE-27**, 290–301, 1989.

[12] Evans, D. L., T. G. Farr, J. P. Ford, T. W. Thompson, and C. L. Werner, "Multipolarization radar images for geologic mapping and vegetation discrimination," *IEEE Trans. Geoscience and Remote Sensing,* **GE-24**, 246–257, 1986.

[13] Evans, D. L., T. G. Farr, J. J. van Zyl, and H. A. Zebker, "Imaging radar polarimetry: Analysis tools and applications," *IEEE Trans. Geoscience and Remote Sensing,* **GE-26**, 774–789, 1988.

[14] Foo, B. Y., S. K. Chaudhuri, and W. M. Boerner, "A high frequency inverse scattering model to recover the specular point curvature from polarimetric scattering matrix data," *IEEE Trans. Antennas and Propagat.,* **AP-32**, 1174–1178, 1984.

[15] Giuli, D., "Polarization diversity in radars," *Proceedings of the IEEE,* **74**(2), 245–269, 1986.

[16] Goodenough, D. C., and C. Livingstone, "Airborne multifrequency, multipolarization SAR, the CCRS experience," *1985 International Geoscience and Remote Sensing Symposium Digest,* 1985.

[17] Hagfors, T., "A study of the depolarization of lunar echoes," *Radio Science,* **2**, 445–465, 1967.

[18] Hunter, I. M., and T. B. A. Senior, "Experimental studies of sea - surface effects on low-angle radars," *Proceedings of the IEEE,* **54**, 1731–1740, 1966.

[19] Huynen, J. R., "Measurement of the target scattering matrix," *Proceedings of the IEEE,* **53**, 936–946, 1965.

[20] Huynen, J. R., *Phenomenological theory of radar targets,* Ph.D. Dissertation, Drukkerij Bronder-Offset, N.V., Rotterdam, 1970.

[21] Huynen, J. R., F. McNolty, and E. Hanson, "Component distribution for fluctuating radar targets," *IEEE Trans. Aerospace and Electronic Systems,* **AES-11**, 1316-1332, 1975.

[22] Huynen, J. R., Phenomenological theory of radar targets, in *Electromagnetic Scattering,* P.L.E. Uslerghi, Ed., Academic Press, New York, 1978.

[23] Ioannidids, G. A., and D. E. Hammers, "Optimum antenna polarizations for target discrimination in clutter," *IEEE Trans. Antennas Propagat.,* **AP-27**, 357-363, 1979.

[24] Jackson, J. D., *Classical Electrodynamics,* John Wiley and Sons, New York, 1976.

[25] Kales, M. L., "Part III - Elliptical polarized waves and antennas," *Proceedings of the IRE,* **39**, 544–549, 1951.

[26] Kennaugh, E. M., "Effects of the type of polarization on echo characteristics," Report 389-9, Antenna Laboratory, Ohio State University, 1951.

[27] Kong, J. A., A. A. Swartz, and H. A. Yueh, "Identification of terrain cover using the optimum polarimetric classifier," *Journal of Electromagnetic Waves and Applications,* 1987.

[28] Kostinski, A. B., and W. M. Boerner, "On foundations of radar polarimetry," *IEEE Trans. on Antennas Propagat.,* **AP-34**, 1395–1404, 1986.

[29] Kozma, A., A. D. Nichols, R. F. Rawson, S. J. Shackman, C. W. Haney, and J. J. Shanne, Multifrequency-Polarimetric SAR for Remote Sensing, *Proceedings of the IGARSS'86 Symposium*, ESA SP-254, 715–720, 1986.

[30] Lim, H. H., A. A. Swartz, H. A. Yueh, J. A. Kong, R. T. Shin, and J. J. van Zyl, "Classification of earth terrain using polarimetric synthetic aperture radar images," *Journal of Geophysical Research,* **94**, No. B6, 7049–7057, 1989.

[31] Long, M. W., "On the polarization and the wavelength dependence of sea echo," *IEEE Trans. Antennas Propagat.,* **AP-13**, 749–754, 1965.

[32] Long, M. W., and S. P. Zehner, "Effect of the sea on echo from rain," *IEEE Trans. Aerospace and Electronic Systems,* **AES-6**,

821–824, 1970.

[33] Peake, W. H., "Theory of radar return from terrain," *IRE National Conference Record*, **7**, Part I, 27–41, 1959.

[34] Rice, S. O., "Reflection of electromagnetic waves from slightly rough surfaces, *Communications of Pure and Applied Mathematics*, **4**, 351–378, 1951.

[35] Rumsey, V. H., "Part I - Transmission between elliptically polarized antennas," *Proceedings of the IRE*, **39**, 535–540, 1951.

[36] Sinclair, G., "The transmission and reception of elliptically polarized waves," *Proceedings of the IRE*, **38**, 148–151, 1950.

[37] Swartz, A. A., H. A. Yueh, J. A. Kong, L. M. Novak, and R. T. Shin, "Optimal polarizations for achieving maximum contrast in radar images," *Journal of Geophysical Research*, **93**, No. B12, 15252–15260, 1988.

[38] Thompson, T. W., A user's guide for the NASA/JPL synthetic aperture radar and the NASA/JPL L- and C- band scatterometers, JPL publication no. 83-38, 1986.

[39] Tsang, L., J. A. Kong, and R. T. Shin, *Theory of Microwave Remote Sensing*, Wiley & Sons, New York, 1985.

[40] Ulaby, F. T., D. N. Held, M. C. Dobson, K. C. McDonald, and T. B. A. Senior, "Relating polarization phase difference of SAR signals to scene properties," *IEEE Trans. Geoscience and Remote Sensing*, **GE-25**, 83-92, 1987.

[41] Ulaby, F. T., K. Sarabandi, K. McDonald, M. Whitt, and M. C. Dobson, "Michigan microwave canopy scattering model," Report 022486-T-1, Radiation Laboratory, University of Michigan, 1988.

[42] Valenzuela, G. R., "Depolarization of EM waves by slightly rough surfaces," *IEEE Trans. Antennas and Propagation*, **AP-15**(4), 552–557, 1967.

[43] Van de Hulst, H. C., *Light Scattering by Small Particles*, 28–42, Dover, New York, 1981.

[44] van Zyl, J. J., On the Importance of Polarization in Radar Scattering Problems, Ph.D. Thesis, Caltech Antenna Laboratory Report No. 120, 152 pp., California Institute of Technology, Pasadena, CA, 1985.

[45] van Zyl, J. J., H. A. Zebker, and C. Elachi, "Imaging radar polarization signatures: Theory and observation," *Radio Science,* **22**, 529–543, 1987.

[46] van Zyl, J. J., "Unsupervised classification of scattering behavior using radar polarimetry data," *IEEE Trans. Geoscience and Remote Sensing,* **GE-27**, 36–45, 1989.

[47] Yueh, H. A., A. A. Swartz, J. A. Kong, R. T. Shin, and L. M. Novak, "Bayes classification of terrain cover using normalized polarimetric data," *Journal of Geophysical Research,* **93**, No. B12, 15261–15267, 1988.

[48] Zebker, H. A., J. J. van Zyl, and D. N. Held, "Imaging radar polarimetry from wave synthesis," *Journal of Geophysical Research,* **92**, No. B1, 683–701, 1987.